Topology optimization of geometrically nonlinear structures using reduced-order modeling

Zhang, Lidan; Zhang, Yi; van Keulen, Fred

DOI
10.1016/j.cma.2023.116371

Publication date
2023

Document Version
Final published version

Published in
Computer Methods in Applied Mechanics and Engineering

Citation (APA)
Zhang, L., Zhang, Y., & van Keulen, F. (2023). Topology optimization of geometrically nonlinear structures using reduced-order modeling. *Computer Methods in Applied Mechanics and Engineering*, *416*, Article 116371. https://doi.org/10.1016/j.cma.2023.116371

Available online at www.sciencedirect.com

ScienceDirect

Comput. Methods Appl. Mech. Engrg. 416 (2023) 116371

Computer methods in applied mechanics and engineering

www.elsevier.com/locate/cma

Topology optimization of geometrically nonlinear structures using reduced-order modeling

Lidan Zhang*, Yi Zhang, Fred van Keulen

Delft University of Technology, Faculty of Mechanical, Maritime and Material Engineering, Mekelweg 2, 2628CD, Delft, The Netherlands

Received 16 June 2023; received in revised form 9 August 2023; accepted 10 August 2023
Available online xxxx

Abstract

High computational costs are encountered in topology optimization problems of geometrically nonlinear structures since intensive use has to be made of incremental-iterative finite element simulations. To alleviate this computational intensity, reduced-order models (ROMs) are explored in this paper. The proposed method targets ROM bases consisting of a relatively small set of base vectors while accuracy is still guaranteed. For this, several fully automated update and maintenance techniques for the ROM basis are investigated and combined. In order to remain effective for flexible structures, path derivatives are added to the ROM basis. The corresponding sensitivity analysis (SA) strategies are presented and the accuracy and efficiency are examined. Various geometrically nonlinear examples involving both solid as well as shell elements are studied to test the proposed ROM techniques. Test cases demonstrates that the set of degrees of freedom appearing in the nonlinear equilibrium equation typically reduces to several tenth. Test cases show a reduction of up to 6 times fewer full system updates.

Keywords: Topology optimization; Geometric nonlinearity; Reduced-order modelings; Shells; Compliant mechanisms

1. Introduction

Topology optimization methods are highly-efficient structural design techniques which can assist in the development of new design principles in innovative sectors of industry. Mainstream topology optimization methods include SIMP [1], level set-based methods [2], ESO methods [3], BESO methods [4], and MMC (moving morphable components) methods [5]. In the present work, we mainly focus on topology optimization using the SIMP method.

The majority of studies on topology optimization of mechanical structures assumes linear elastic material behavior and geometric linearity. Indeed, these simplifications are suitable for a large class of problems. However, for specific classes, it is necessary to account for geometric nonlinearity in the analysis. Typically examples are thin-walled structures [6,7], compliant mechanisms [8,9], and multi-stable structures with snap-through behavior [10]. Consequently, seeking efficient and effective methods to carry out topology optimization for structures exhibiting geometric nonlinearity is of great practical relevance.

Several aspects cause topology optimization of geometrically nonlinear structures to be challenging. Compared with their linear counterparts, nonlinear structural optimization problems are computationally expensive since

* Corresponding author.
E-mail addresses: l.zhang-5@tudelft.nl (L. Zhang), zhangyi413@outlook.com (Y. Zhang), A.vanKeulen@tudelft.nl (F. van Keulen).

https://doi.org/10.1016/j.cma.2023.116371

intensive use has to be made of incremental-iterative finite element simulations [11]. Besides, when deflections and rotations become finite, although deformations may still be small, void elements in the design space may get severely distorted and even "inverted", causing the tangent stiffness matrices to be indefinite and/or ill-conditioned, which may easily spoil the convergence of the nonlinear finite element analysis. This leads to catastrophic failure of the overarching optimization process [12–14]. Furthermore, like topology optimization of eigen frequencies or buckling loads, spurious modes will occur in low-density areas. The low-density areas are very flexible as compared to areas with full densities, and may therefore control the lowest eigenmodes of the whole structure [15,16]. In the present work, we primarily focus on the reduction of the computational burden associated with topology optimization when geometrically nonlinearity is considered. Potentially, reduced-order models (ROMs) are powerful strategies to deal with such problems.

ROMs attempt to use a small number of generalized variables to approximate the behavior governed by a large number of degrees of freedom (DOFs) associated with the full-order model (FOM). Each generalized variable corresponds to a base vector which can be a natural frequency mode, buckling mode, a static displacement field among others [17–19]. The computational costs of a ROM depend heavily on the number of base vectors and effort to create the basis. ROMs are potentially valuable for the incremental-iterative solution of large-scale problems, as encountered in structural nonlinear analysis. Chan and Hsiao [19] used the solution vectors and correction vectors generated during a modified Newton process as base vectors for nonlinear static analysis. Safjan [20] not only used correction vectors but also the lowest eigenvectors of updated tangent stiffness matrices. Kim et al. [21] constructed ROMs for nonlinear structural dynamic analysis of isotropic and functionally graded plates. They combined linear FOM solutions with additional nonlinear FOM static solutions, so-called "dual modes", which were generated by applying a series of representative static loads on the structure.

In topology optimization, various applications of ROMs have been reported for linear settings. Amir et al. [22] applied a ROM for approximate reanalysis in topology optimization of linear structures. They demonstrated that relatively rough approximations were acceptable in analysis since a consistent ROM-based sensitivity evaluation was applied, in which the errors caused by the ROM are taken into account. Gogu [23] applied ROMs for topology optimization of linear structures and enriched the ROM basis with previously calculated solutions. Hooijkamp and van Keulen [24] focused on topology optimization for linear transient thermomechanical problems. A reduced thermal modal basis augmented with static correction was used to replace the tedious backward transient integration by analytical convolutions in the adjoint sensitivity analysis. Wang et al. [25] investigated large-scale three-dimensional linear topology optimization problems. They used the Krylov subspace method combined with preconditioning techniques to solve the optimization problems and reduce the computing burden by recycling selected search spaces from previously analyzed linear systems.

For ROM-based topology optimization in nonlinear settings, a few publications related to material nonlinearity can be found. For instance, Xia and Breitkopf [26] presented a reduced multiscale model for macroscopic structural design considering material nonlinear microstructures. The ROM model uses Proper Orthogonal Decomposition (POD) and Diffuse Approximation to replace the detailed microscopic finite element analysis. However, for geometric nonlinearity, publications can only be found in size and shape optimization problems, but for topology optimization. For example, for size optimization, Orozco and Ghattas [27] used ROMs to reduce the SQP-based simultaneous analysis and design (SAND) problem taking into account geometric nonlinearity. The resulting reduced problem has the same size as the nested analysis and design (NAND) problem but achieves higher efficiency. Given the promising results obtained in previous work, it is concluded that ROMs have great potential in topology optimization for geometrically nonlinear structures. Nevertheless, ROMs have never been introduced in this field.

In this paper, ROMs are applied to topology optimization problems for geometrically nonlinear structures aiming at enhancing the computational efficiency of the associated incremental-iterative finite element simulations and the corresponding sensitivity analysis. The proposed ROMs target a relatively small set of base vectors while the accuracy can still be guaranteed. For this, several fully automated update and maintenance strategies for the ROM basis are investigated and combined. Besides, approximated ROM-based sensitivity analysis strategies (ARSA) are presented and the accuracy of the SA strategies are examined and compared to consistent FOM-based sensitivity analysis (CFSA). In addition, a formulation of consistent ROM-based sensitivity analysis (CRSA) is presented in the paper. However, no numerical tests are conducted for CRSA, since this sensitivity is rather unpractical for the updating techniques presented in this work. Finally, various geometrically nonlinear examples involving solid or shell elements are studied to test the proposed ROM-based topology optimization techniques.

This paper is organized as follows. In Section 2, the general formulation of geometrically nonlinear topology optimization is summarized. In Section 3, ROM-based finite element analysis strategies are discussed. Section 4 presents different updating and maintenance techniques of ROMs for geometrically nonlinear topology optimization. Section 5 introduces the corresponding approximated ROM sensitivity analysis techniques for geometrically nonlinear structures. Section 6 provides several numerical experiments. ARSA is compared to CFSA and ROM-based optimization results are compared with those using FOMs. Finally, conclusions are given in Section 7.

2. Geometrically nonlinear topology optimization

Topology optimization formulations associated with an objective function J, inequality constraints $\mathbf{h}$, design variables (pseudo densities) $\boldsymbol{\rho}$ and their corresponding lower bounds $\boldsymbol{\rho}_{\min}$ can be expressed by

$$\begin{aligned} &\min_{\boldsymbol{\rho}} \ J\left[\mathbf{d}\left[\boldsymbol{\rho}\right], \boldsymbol{\rho}\right], \\ &\text{s.t.}: \mathbf{h}\left[\mathbf{d}\left[\boldsymbol{\rho}\right], \boldsymbol{\rho}\right] \leq \mathbf{0}, \\ &\quad \mathbf{0} < \boldsymbol{\rho}_{\min} \leq \boldsymbol{\rho} \leq \mathbf{1}. \end{aligned} \tag{1}$$

Here "[$*$]" denotes the function of "$*$", $\mathbf{d}$ represents mechanical responses, i.e. nodal degrees of freedom. Lower bounds $\boldsymbol{\rho}_{\min}$ are typically set to avoid singularity caused by removing material.

In many cases, simplifying topology optimization to a linear setting is sufficient to achieve a good and reasonable design. However, the linearity assumption is too restrictive for designs involving flexible structures exposed to finite rotations and/or for which geometric stiffness plays a crucial role. These structures often exhibit finite deflections and rotations, although the deformations remain small. Thus, it is paramount to consider geometric nonlinearity to ensure the final design functions correctly.

The geometrically nonlinear equilibrium equations are formulated using the virtual work principle

$$\delta W^{\text{int}} = \delta W^{\text{ext}}. \tag{2}$$

Here, δW^{ext} is the external virtual work and δW^{int} represents the internal virtual work. In a discrete setting, the external virtual work can be expressed by

$$\delta W^{\text{ext}} = \mathbf{f}^{\mathrm{T}} \delta \mathbf{d}, \tag{3}$$

where $\mathbf{f}$ represents the external nodal loads. In order to avoid all finite element details, we shall introduce generalized deformations and stresses. Their precise definition depends on the finite elements at hand and their implementation. The internal virtual work in a discrete form can be expressed by

$$\delta W^{\text{int}} = \boldsymbol{\sigma}^{\mathrm{T}} \delta \boldsymbol{\epsilon}, \tag{4}$$

where $\boldsymbol{\sigma}$ represents the generalized stresses and $\boldsymbol{\epsilon}$ the generalized deformations, with $\boldsymbol{\epsilon}[\mathbf{d}]$. Given the geometrically nonlinear setting, $\boldsymbol{\epsilon}[\mathbf{d}]$ is nonlinear in $\mathbf{d}$. For the variations of $\boldsymbol{\epsilon}$ it follows

$$\delta \boldsymbol{\epsilon} = \mathbf{D}\left[\mathbf{d}\right] \delta \mathbf{d}, \tag{5}$$

where the components of $\mathbf{D}$ are determined by

$$D_{ij} = \frac{\partial \epsilon_i}{\partial d_j}. \tag{6}$$

A generalized constitutive relation can be used to express the generalized stresses in terms of the generalized deformations. Since a linear elastic material model is assumed, this general expression can be formulated as

$$\boldsymbol{\sigma} = \mathbf{S} \boldsymbol{\epsilon}, \tag{7}$$

where $\mathbf{S}$ is the generalized constitutive matrix. At element level, the matrices corresponding to $\mathbf{D}$ and $\mathbf{S}$ are denoted by $\mathbf{D}_e$ and $\mathbf{S}_e$.

In the SIMP method [1], the constitutive matrix is scaled at element level with element density ρ_e:

$$\mathbf{S}_e \rightarrow \rho_e^p \mathbf{S}_e. \tag{8}$$

Here parameter p is used to penalize intermediate densities. A low value of p results in more intermediate density elements, while a high value of p results in a less convex optimization problem but more crisp designs. Usually, $p = 3$ is adopted [1].

Starting from Eq. (2), the equilibrium equation can be expressed as

$$\mathbf{D}^{\mathrm{T}}[\mathbf{d}]\boldsymbol{\sigma} - \mathbf{f} = \mathbf{q}[\mathbf{d}] - \mathbf{f} = \mathbf{0}, \tag{9}$$

where $\mathbf{q} = \mathbf{D}^{\mathrm{T}}\boldsymbol{\sigma}$ represents the so-called "internal" load.

To solve the governing equations, an incremental-iterative method is applied in the present work. For this, a load factor λ is introduced. Thus, the external load $\mathbf{f}$ is written as a function of λ. Then, the equilibrium equation reads

$$\mathbf{q}[\mathbf{d}] - \mathbf{f}[\lambda] = 0. \tag{10}$$

Next, the corresponding rate equations follow as

$$\mathbf{K}_{\mathrm{T}}[\mathbf{d}]\frac{\mathrm{d}\mathbf{d}}{\mathrm{d}\lambda} - \frac{\mathrm{d}\mathbf{f}}{\mathrm{d}\lambda} = 0, \tag{11}$$

with the $l \times l$ tangent stiffness matrix $\mathbf{K}_{\mathrm{T}}$ being defined as

$$\mathbf{K}_{\mathrm{T}} = \frac{\partial \mathbf{q}[\mathbf{d}]}{\partial \mathbf{d}}. \tag{12}$$

where l is the number of structural DOFs. Then, the incremental technique starting from load step i to $i+1$ can be formulated as

$$\mathbf{d}^{i+1} = \mathbf{d}^{i} + \left(\mathbf{K}_{\mathrm{T}}\left[\mathbf{d}^{i}\right]\right)^{-1}\left(\mathbf{f}\left[\lambda^{i+1}\right] - \mathbf{q}\left[\mathbf{d}^{i}\right]\right). \tag{13}$$

After the load incremental has been applied, classical Newton iterations are carried out to obtain the corresponding nonlinear solution. For a specific load level $\lambda^{i+1} = \lambda^{c}$, the Newton iterations follow as

$$\mathbf{d}_{j+1} = \mathbf{d}_{j} + \left(\mathbf{K}_{\mathrm{T}}\left[\mathbf{d}_{j}\right]\right)^{-1}\left(\mathbf{f}\left[\lambda^{c}\right] - \mathbf{q}\left[\mathbf{d}_{j}\right]\right). \tag{14}$$

Here superscripts are used to identify the different load levels, whereas subscripts are used to indicate Newton iterations at a constant load level. The Newton iterations are continued until the convergence criterion is satisfied. The latter is defined by the norm of the residual:

$$e_f = \frac{\|\mathbf{f}[\lambda^{c}] - \mathbf{q}\left[\mathbf{d}_{j+1}\right]\|}{\|\mathbf{f}[\lambda^{c}]\|} \leq \epsilon_f. \tag{15}$$

Here e_f denotes the imbalance error, ϵ_f a user-defined tolerance, and $\|*\|$ represents a norm. The latter for a vector $\mathbf{x} = [x_1, x_2, \ldots, x_w]$, in this work, is denoted by $\|\mathbf{x}\| = \sqrt{x_1^2 + x_2^2 + \cdots + x_w^2}$. Here w stands for the dimension, which is the number of structural nodal DOFs in Eq. (15).

If the convergence criterion Eq. (15) is satisfied, the Newton iterations are converged. After convergence for a particular load level, we move to the next load step and the corresponding nonlinear solution is obtained again iteratively. As observed, since intensive use has to be made of incremental-iterative finite element simulations, the solution may be very expensive particularly when the number of nodal degrees of freedom, gets large. Especially in optimization, this become problematic because a large number of nonlinear problems has to be solved during the design process. In order to enhance efficiency, reduced-order modeling is introduced in the next section.

3. ROM-based finite element analysis

Ritz' method is used to reduce the kinematic DoFs. For this, the nodal degrees of freedom are approximated by

$$\overline{\mathbf{d}} = \mathbf{R}\mathbf{y}, \tag{16}$$

where $\overline{\mathbf{d}}$ denotes the approximate nodal degrees of freedom for the full-order model and $\mathbf{y}$ are generalized coordinates. The matrix $\mathbf{R}$ represents the ROM basis

$$\mathbf{R} = [\boldsymbol{\phi}_1, \boldsymbol{\phi}_2, \ldots, \boldsymbol{\phi}_m], \tag{17}$$

where m is the number of base vectors and $\boldsymbol{\phi}_i$ denotes an individual base vector. In order to obtain an efficient ROM, it is essential that the number of base vectors (m) is significantly smaller than the number of nodal degrees of freedom (l). Using Ritz' method, the ROM-based governing equation can be expressed as

$$\mathbf{R}^{\mathrm{T}}(\mathbf{q}\left[\overline{\mathbf{d}}\right] - \mathbf{f}) = \mathbf{0}. \tag{18}$$

Here,

$$\mathbf{q}\left[\overline{\mathbf{d}}\right] = \mathbf{D}^{\mathrm{T}}\left[\overline{\mathbf{d}}\right]\boldsymbol{\sigma}\left[\overline{\mathbf{d}}\right] = \mathbf{D}^{\mathrm{T}}\left[\mathbf{R}\mathbf{y}\right]\left(\mathbf{S}\boldsymbol{\epsilon}\left[\mathbf{R}\mathbf{y}\right]\right). \tag{19}$$

The corresponding rate equations follow as

$$\left(\overline{\mathbf{K}}_{\mathrm{T}}\left[\mathbf{y}\right]\right)^{-1}\frac{\mathrm{d}\mathbf{y}}{\mathrm{d}\lambda} - \frac{\mathbf{R}^{\mathrm{T}}\mathbf{f}}{\mathrm{d}\lambda} = \mathbf{0}, \tag{20}$$

with $\overline{\mathbf{K}}_T$ representing the $m \times m$ reduced tangent stiffness matrix, which is expressed by full tangent stiffness matrix $\mathbf{K}_{\mathrm{T}}\left[\overline{\mathbf{d}}\right]$, i.e. $\mathbf{K}_{\mathrm{T}}\left[\mathbf{R}\mathbf{y}\right]$, and ROM basis $\mathbf{R}$:

$$\overline{\mathbf{K}}_{\mathrm{T}}\left[\mathbf{y}\right] = \mathbf{R}^{\mathrm{T}}\mathbf{K}_{\mathrm{T}}\left[\mathbf{R}\mathbf{y}\right]\mathbf{R}. \tag{21}$$

Here, the right-hand term can be assembled element-by-element:

$$\mathbf{R}^{\mathrm{T}}\mathbf{K}_{\mathrm{T}}\left[\mathbf{R}\mathbf{y}\right]\mathbf{R} = \mathop{\mathsf{A}}_{e}\mathbf{R}_e^{\mathrm{T}}\mathbf{K}_{\mathrm{T}}^{e}\left[\mathbf{R}\mathbf{y}\right]\mathbf{R}_e. \tag{22}$$

Here, $\mathbf{R}_e$ and $\mathbf{K}_{\mathrm{T}}^{e}$ are corresponding matrices at element level.

As in the FOM setting, an incremental-iterative method can be applied to solve the nonlinear reduced governing equations. For a specific load step $\lambda^{i+1} = \lambda^{\mathrm{c}}$, the ROM-based Newton iterations can be expressed as

$$\mathbf{y}_{j+1} = \mathbf{y}_j + \triangle\mathbf{y}_{j+1}, \tag{23}$$

with

$$\Delta\mathbf{y}_{j+1} = \left(\overline{\mathbf{K}}_{\mathrm{T}}\left[\mathbf{y}_j\right]\right)^{-1}\mathbf{R}^{\mathrm{T}}\left(\mathbf{f}\left[\lambda^c\right] - \mathbf{q}\left[\mathbf{R}\mathbf{y}_j\right]\right). \tag{24}$$

As can be seen from Eqs. (23) and (24), Newton iterations are based on the reduced tangent stiffness matrix. This contributes to the computational efficiency since the dimensions of the latter depends on the number of base vectors, which is much smaller than the number of structural DOFs. The ROM-based Newton iterations for a specific load step are continued until a ROM-based convergence criterion is met. The latter is defined by using the norm of the reduced residual:

$$e_r = \frac{\|\mathbf{R}^{\mathrm{T}}\left(\mathbf{f}\left[\lambda^c\right] - \mathbf{q}\left[\mathbf{R}\mathbf{y}_{j+1}\right]\right)\|}{\|\mathbf{R}^{\mathrm{T}}\mathbf{f}\left[\lambda^c\right]\|} \le \epsilon_r. \tag{25}$$

Here, e_r denotes the imbalance error and ϵ_r a user-defined tolerance. The dimensions of $\mathbf{R}^{\mathrm{T}}\left(\mathbf{f}\left[\lambda^c\right] - \mathbf{q}\left[\mathbf{R}\mathbf{y}_{j+1}\right]\right)$ and $\mathbf{R}^{\mathrm{T}}\mathbf{f}\left[\lambda^c\right]$ equal the number of base vectors.

After the ROM-based Newton iterations have converged, we get $\mathbf{y}^{\mathrm{c}}$ corresponding to λ^c. Next, we project $\mathbf{y}^{\mathrm{c}}$ to get the ROM-based solution $\overline{\mathbf{d}}^{\mathrm{c}}$ for the nodal degrees of freedom by Eq. (16), and then assess its accuracy. If the solution $\overline{\mathbf{d}}^{\mathrm{c}}$ is accurate, then it should also satisfy the full system equilibrium equation. This implies that the norm of the full-system based residual, $\|\mathbf{f}\left[\lambda^c\right] - \mathbf{q}\left[\overline{\mathbf{d}}^{\mathrm{c}}\right]\|$, should be sufficiently small. Hence, an error measure based on the full-system residual is proposed as

$$\eta = \frac{\|\mathbf{f}\left[\lambda^c\right] - \mathbf{q}\left[\overline{\mathbf{d}}^{\mathrm{c}}\right]\|}{\|\mathbf{f}\left[\lambda^c\right]\|}. \tag{26}$$

Here, the dimensions of $\mathbf{f}\left[\lambda^c\right] - \mathbf{q}\left[\overline{\mathbf{d}}^{\mathrm{c}}\right]$ and $\mathbf{f}\left[\lambda^c\right]$ equal the number of structural nodal DOFs.

If η is smaller than a user defined tolerance δ_s, then the ROM-based solution is considered accurate. Otherwise, the ROM-based solution, though well converged, is considered inaccurate and needs to be improved. For this, correction strategies and techniques to construct, update, and maintain the ROM basis are introduced in the next section.

4. ROM basis

One of the most critical ingredient of the ROM is the choice of an appropriate set of base vectors. Effectively, the required set may depend on both the current load level (λ^c), as well as on the structure, i.e. the design at hand. An ideal set of base vectors should be linearly independent, requiring low computational cost for its generation, and sufficiently complete to capture the nonlinear response of the structure. In addition, the number of base vectors should be limited to ensure a small ROM basis. To meet the aforementioned requirements, firstly, orthogonalization is applied to ensure linear independence (Details are provided in Appendix A). Secondly, the ROM basis is initiated using FOM-based solutions. Thirdly, to ensure accuracy, FOM-based correction technique is adopted. The initialization and the correction are provided in Section 4.1. Next, the ROM basis is augmented on the basis of FOM-based solutions evaluated for previous designs. The details of this augmentation are described in Section 4.2. In order to ensure the ROM basis remains compact, maintenance strategies are presented in Section 4.3.

4.1. Initialization and error control

At the very beginning of the optimization, i.e. at the first load step of the first optimization step, the ROM basis is empty. Hence, the optimization is initiated using the full-order model. As reported in [19], including the converged nonlinear solution and correction solutions obtained during Newton iterations constitute good ingredients for a ROM-based nonlinear static analysis. In our practice, correction solutions of iterations do not effectively contribute to the accuracy of ROMs, but increase the number of base vectors. Hence, in the proposed scheme, we exclusively add the first converged nonlinear FOM solution, but also consider the first predictor solution, i.e. the FOM solution to the linearized governing equation in the undeformed configuration. Following that, a ROM basis with these two vectors can be used to generate a ROM-based solution for the next load step.

After convergence of a ROM-based analysis, the accuracy of the solution is evaluated using Eq. (26), which is the full-order residual, but evaluated for the ROM-based solution. If the solution is accurate enough, i.e. $\eta \leqslant \delta_s$, then no correction is required and the current ROM solution will be accepted. If the error is too large, i.e. $\eta > \delta_s$, a correction is applied to eliminate the error. For this, starting from the present ROM-based solution, FOM-based Newton iterations are conducted. Subsequently, the resulting converged FOM-based solution is regarded as the final result for the current load step. It is obvious that the correction based on the full system is relatively time-consuming. Thus, improving the accuracy of ROMs to reduce computing time for FOM-based corrections is essential for efficiency. Consequently, before proceeding to the next load step, the resulting FOM-based nonlinear solution is added to the ROM basis. Hence, the next load step will be based on the updated ROM basis. The extension of the ROM basis is restricted by a maximum number of base vectors. If the ROM basis has reached the maximum number of base vectors, then specific base vectors will be removed from the basis. The details are provided in Section 4.3.

4.1.1. Path derivatives for flexible structures

A ROM basis, as described in the previous subsection, is accurate for most cases except for very flexible structures like structures exhibiting nearly inextensional bending. In these cases, the flexible bending mode is typically badly represented by the existing basis, leading to ROM-based responses which are far too stiff. To grasp this concept more easily, consider a cantilever beam subjected to pure bending. When the deformation is correctly captured in a nonlinear manner, we observe that the beam can bend into a circle. This circular shape indicates that the beam's tip experiences both out-of-plane and in-plane deflections. In contrast, a poorly represented flexible bending mode would exhibit insufficient in-plane deflection, i.e. excessive in-plane stiffness. One extreme case of the later is a linear mode where no in-plane deflection appears. One solution for the issue is to introduce curvature information on the load–deflection path, i.e. 2nd-order path derivatives. Such derivatives add information on the flexible bending modes. More explanations can be found in Appendix B. In this section, the method of adding curvature information is presented.

The 2nd-order path derivatives can be approximated by forward finite-differences

$$\frac{\mathrm{d}^2\mathbf{d}}{\mathrm{d}\lambda^2} = \frac{\mathbf{d}^* - 2\mathbf{d}^*_{\Delta\lambda^*} + \mathbf{d}^*_{2\Delta\lambda^*}}{(\Delta\lambda^*)^2}. \tag{27}$$

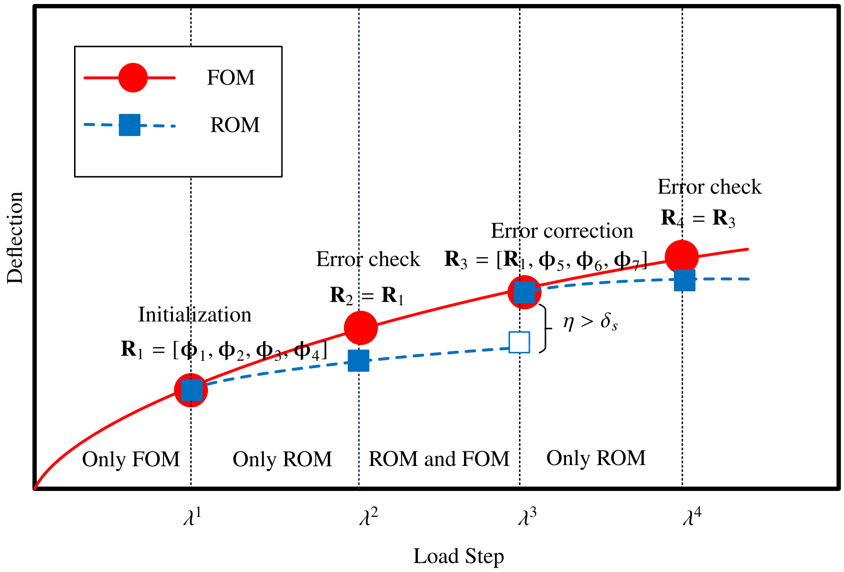

Fig. 1. Initialization and accuracy control for ROMs. The red line represents schematically the FOM-based solutions, the blue line the ROM-based solution, $\mathbf{R}_i$ denotes the ROM basis corresponding to load level λ^i, $\boldsymbol{\phi}_m$ are base vectors, and δ_s is a user-defined error tolerance. Initialization is applied at the first load level (λ^1) where $\boldsymbol{\phi}_1$ denotes the linear FOM solution, $\boldsymbol{\phi}_2$ the FOM-based nonlinear solution, $\boldsymbol{\phi}_3$ and $\boldsymbol{\phi}_4$ perturbation solutions. Error checking is performed for each ROM-based solution. In the above illustration, for load level (λ^2), the error is acceptable and, thus, no FOM-based correction is applied. Consequently, $\mathbf{R}^2$ is used for load level (λ^3). However, for load level (λ^3), too large an error is detected and a FOM-based correction is conducted and the ROM basis is extended by $\boldsymbol{\phi}_5$, the FOM-based nonlinear solution, as well as by $\boldsymbol{\phi}_6$ and $\boldsymbol{\phi}_7$. The latter follows from the corresponding perturbations. Subsequently, the same logic as for (λ^2) is applied for (λ^4).

Here, $\mathbf{d}^*$ denotes a FOM-based solution corresponding to the current load level λ^*, $\Delta\lambda^*$ a small perturbation of the load factor λ^*, $\mathbf{d}^*_{\Delta\lambda^*}$ and $\mathbf{d}^*_{2\Delta\lambda^*}$ are FOM-based perturbation solutions corresponding to perturbed load levels $(\lambda^* + \Delta\lambda^*)$ and $(\lambda^* + 2\Delta\lambda^*)$, respectively. Given the introduced orthonormalization (see Appendix A), a practical approach to include the information on the 2nd-order path derivative is by simply adding $\mathbf{d}^*$, $\mathbf{d}^*_{\Delta\lambda^*}$, and $\mathbf{d}^*_{2\Delta\lambda^*}$ as new base vectors. Note, the FOM-based solution $\mathbf{d}^*$ has already been added to the basis. Starting from λ^*, the load factor is perturbed twice to get $\mathbf{d}^*_{\Delta\lambda^*}$ and $\mathbf{d}^*_{2\Delta\lambda^*}$. It is deserved to mention that including only $\mathbf{d}^*_{\Delta\lambda^*}$ is equivalent to adding current tangent information of the path. This can also contribute the accuracy to some extend. But for very flexible structures, the curvature information is highly desired to ensure the accuracy, which can be roughly achieved by adding $\mathbf{d}^*_{2\Delta\lambda^*}$. Here, we use the perturbation step $\Delta\lambda^* = \Delta\lambda \times 10^{-3}$, i.e. $\Delta\lambda^*$ is selected as a small fraction of the applied load step $\Delta\lambda$, which, based on our test cases, is effective. Since $\Delta\lambda^*$ is very small, modified Newton iterations can be employed to keep the updating computationally efficient, where the tangent stiffness matrix corresponding to λ^* is used for both steps. By adding $\mathbf{d}^*_{\Delta\lambda^*}$ and $\mathbf{d}^*_{2\Delta\lambda^*}$, we efficiently add information on the curvature of the loading path, thus improving the accuracy of the corresponding ROM-based solutions. For one optimization step, the strategy is schematically illustrated in the Fig. 1, where $\mathbf{R}_i$ represents the ROM basis of load step i.

4.2. Augmentation technique

In the previous sections, we described the ROM updating strategy for the first step in the optimization. Such a method, in which we construct the ROM basis from scratch, can also be applied to subsequent optimization steps. However, this would disregard the potential benefits of FOM-based solutions evaluated for previous designs. The FOM-based solutions can be stored and could provide an accurate prediction of a slightly adapted design. To maximize the use of previous FOM-based solutions, i.e. previous ROM bases, we propose an augmentation technique in this section.

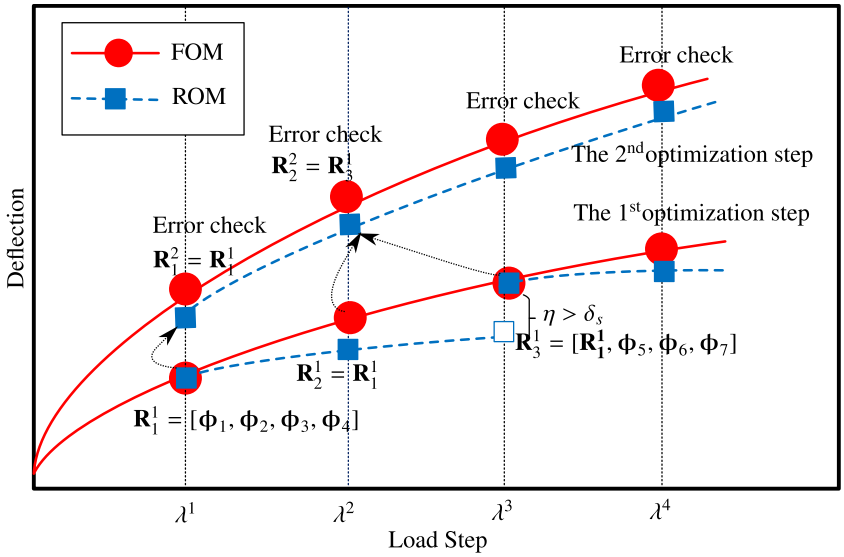

Fig. 2. Augmentation of ROM basis where the red lines represent the FOM-based solutions, the blue lines the ROM-based solutions, $\mathbf{R}_i^k$ denotes the ROM basis corresponding to load level λ^i in optimization step k, $\boldsymbol{\phi}_m$ are base vectors, and δ_s is a user-defined error tolerance. When $k = 1$, the same logic as described in Section 4.1 applies. For $(k = 2, i = 1)$, instead of initializing the ROM basis with FOMs, we take $\mathbf{R}_1^1$ as the current ROM basis. Then, similar to the first optimization iteration, error checking is applied to the ROM-based solution. Since the error in this example is acceptable, no FOM-based correction is applied. Hence, at $\left(k = 2, \lambda^1\right)$, we have $\mathbf{R}_1^2 = \mathbf{R}_1^1$. Next, before $\mathbf{R}_1^2$ is used for the second load level, it is augmented by previous design's ROM bases $\mathbf{R}_2^1$ and $\mathbf{R}_3^1$. After convergence, the error checking is performed. Since no error correction is applied, at $\left(k = 2, \lambda^2\right)$, we have $\mathbf{R}_2^2 = \mathbf{R}_3^1$. Subsequently, the same strategy is applied to the subsequent load levels and optimization steps. (For interpretation of the references to color in this figure legend, the reader is referred to the web version of this article.)

As an illustration, Fig. 2 depicts the first and second step of an optimization. Here $\mathbf{R}_i^k$ denotes the ROM basis of load step i at optimization iteration k. When $k = 1$, the strategy as described in Section 4.1 applies. For $k > 1$ and $i = 1$, instead of using FOMs for initialization, we directly take $\mathbf{R}_1^{k-1}$ as the current ROM basis to enhance the efficiency. After convergence, error control, as described in Section 4.1, is applied and the ROM basis is updated if too large an error is encountered. When $k > 1$ and $i > 1$, we check the base vectors of load level i and $i + 1$ from the previous optimization iteration $k - 1$. We add these base vectors if they are not included in the current ROM basis. Then, the augmented ROM basis is applied to generate the ROM-based solution for the next load level. Similarly, after convergence, the error control is applied and the ROM basis is updated if necessary.

4.3. Maintenance strategies

As shown, it is advantageous to include new base vectors throughout the optimization. The ROM basis is updated on the one hand to maintain accuracy for different load levels. On the other hand, the ROM basis is adapted to new designs when topology designs change. Given this, it is necessary to limit the maximum number of base vectors in order to maintain compactness of the ROM basis. If the number of base vectors reaches the maximum, old base vectors must be removed from the ROM basis to make room for new vectors. The corresponding strategy is described in this section.

For a ROM basis $\mathbf{R} = [\boldsymbol{\phi}_1, \boldsymbol{\phi}_2, \ldots, \boldsymbol{\phi}_m]$, base vectors from $\boldsymbol{\phi}_1$ to $\boldsymbol{\phi}_m$ are sequentially added to $\mathbf{R}$ following the strategy described in previous subsections. After adding each new vector, we apply the orthogonalization (see Appendix A) to all vectors in the basis. This implies that the base vector added at last, i.e. $\boldsymbol{\phi}_m$, could make very large contributions to the ROM-based solution, whereas, the vector added at first, i.e. $\boldsymbol{\phi}_1$, could make very small contributions. Consequently, when the basis is full and a new vector need to be added, we simply remove the first base vector, i.e. $\boldsymbol{\phi}_1$, in the ROM basis.

Furthermore, if the ROM basis is not full yet, it is possible to reduce the size even further without sacrificing accuracy. This can be done by removing the base vector with the smallest contribution. The contribution c_i of base vector $\boldsymbol{\phi}_i$ can be expressed by

$$c_i =\mid \frac{y_i}{y_{\max}} \mid, \tag{28}$$

where y_i denotes generalized coordinates, " $\mid * \mid$ " means a absolute value, and

$$y_{\max} = \max(y_1, y_2, \ldots, y_m). \tag{29}$$

If $c_{\min} = \min\{c_i\} < \delta_{\text{rej}}$, we then remove the base vector corresponding to $c_{\min}$. Here δ_{rej} denotes a user-defined small value and we use 1×10^{-8} in this work. This method is known as "rejection", which will be applied to all ROM-based load levels where the ROM-based solution is deemed accurate. So far, we have explained all related strategies for initializing, updating, and maintaining the ROM basis. In order to use ROMs for optimization, we still need to deduce the ROM-based sensitivities. More details can be seen in the next section.

5. Design sensitivity analysis

For topology optimization, sensitivity analysis (SA) is essential. The adjoint method is frequently used since the number of design variables is typically much larger than the number of constraints. The adjoint formulation for FOMs is already well-known in the field. Hence, we just summarize it in Section 5.1 and refer to it as consistent FOM sensitivity analysis (CFSA). CFSA will be used when a FOM-based solution is available, e.g. after initialization and error correction. In fact, one could use CFSA for a ROM-based solution, but this would be expensive and, effectively, the resulting sensitivities are not consistent. Consequently, we derive the consistent ROM-based sensitivity analysis (CRSA) in Section 5.2, which requires derivatives of all base vectors. However, owing to our augmentation technique, which involves previous FOM solutions, such derivatives are rather impractical to be considered. Therefore, an approximation is created for the CRSA, and the modified formulation is referred to as the approximate ROM-based sensitivity analysis (ARSA).

5.1. Consistent FOM sensitivity analysis (CFSA)

To deduce the adjoint formulations for the consistent FOM sensitivity, we introduce the equilibrium equation Eq. (10) to the response function J by adjoint variables $\boldsymbol{\theta}$, where $\boldsymbol{\theta}$ is a column, and the augmented response function $\bar{J}$ is

$$\bar{J}\left[\mathbf{d}\left[\boldsymbol{\rho}\right], \boldsymbol{\rho}\right] = J\left[\mathbf{d}\left[\boldsymbol{\rho}\right], \boldsymbol{\rho}\right] + \boldsymbol{\theta}^{\mathrm{T}}\left(\mathbf{f} - \mathbf{q}\left[\mathbf{d}\left[\boldsymbol{\rho}\right], \boldsymbol{\rho}\right]\right). \tag{30}$$

To improve readability, $\mathbf{d}\left[\boldsymbol{\rho}\right]$ is shortly represented by $\mathbf{d}$.

The derivative of $\bar{J}$ with respect to $\boldsymbol{\rho}$ is

$$\frac{\mathrm{d}\bar{J}\left[\mathbf{d}, \boldsymbol{\rho}\right]}{\mathrm{d}\boldsymbol{\rho}} = J_{,\mathbf{d}}\left[\mathbf{d}, \boldsymbol{\rho}\right]\frac{\mathrm{d}\mathbf{d}}{\mathrm{d}\boldsymbol{\rho}} - \boldsymbol{\theta}^{\mathrm{T}}\left(\mathbf{q}_{,\mathbf{d}}\left[\mathbf{d}, \boldsymbol{\rho}\right]\frac{\mathrm{d}\mathbf{d}}{\mathrm{d}\boldsymbol{\rho}} + \mathbf{q}_{,\boldsymbol{\rho}}\left[\mathbf{d}, \boldsymbol{\rho}\right]\right) + J_{,\boldsymbol{\rho}}\left[\mathbf{d}, \boldsymbol{\rho}\right], \tag{31}$$

Here the comma "," represents partial derivatives. From Eq. (31), the computation of the expensive derivatives $\frac{\mathrm{d}\mathbf{d}}{\mathrm{d}\boldsymbol{\rho}}$ can be avoided if the adjoint variables $\boldsymbol{\theta}$ are selected as the solution of

$$\mathbf{K}_{\mathrm{T}}\left[\mathbf{d}, \boldsymbol{\rho}\right]\ \boldsymbol{\theta} = J_{,\mathbf{d}}\left[\mathbf{d}, \boldsymbol{\rho}\right]. \tag{32}$$

Here, one linear solution step need to be conducted. When $\mathbf{K}_T$ is large, its decomposition could be expensive if it is not available. After obtaining $\boldsymbol{\theta}$, the design sensitivity can be calculated by

$$\frac{\mathrm{d}J\left[\mathbf{d}, \boldsymbol{\rho}\right]}{\mathrm{d}\boldsymbol{\rho}} = \frac{\mathrm{d}\bar{J}\left[\mathbf{d}, \boldsymbol{\rho}\right]}{\mathrm{d}\boldsymbol{\rho}} = -\boldsymbol{\theta}^{\mathrm{T}}\mathbf{q}_{,\boldsymbol{\rho}}\left[\mathbf{d}, \boldsymbol{\rho}\right] + J_{,\boldsymbol{\rho}}\left[\mathbf{d}, \boldsymbol{\rho}\right]. \tag{33}$$

Given that $\mathbf{q}_{,\boldsymbol{\rho}}$ is easy to evaluate, the only time-consuming term could be the solution of Eq. (32). In fact, one could use CFSA for a ROM-based solution, but this would be expensive and, effectively, the resulting sensitivities are still not consistent. Consequently, we derive (approximate) ROM-based sensitivity analysis in the next section.

5.2. Consistent ROM-based sensitivity analysis (CRSA) and its approximation (ARSA)

At first, the consistent reduced-order sensitivity analysis (CRSA) is derived. We introduce the ROM-based equilibrium function related to $\bar{\mathbf{d}}$ (See Eq. (18)) to the response function J by adjoint variables $\boldsymbol{\mu}$. Here, $\boldsymbol{\mu}$ is a column. Meanwhile, we also introduce the FOM-based equilibrium function related to base vectors $\boldsymbol{\phi}_j$ (See Eq. (9)) to J by adjoint variables $\boldsymbol{\theta}_j$. Here, $\boldsymbol{\theta}_j$ is also a column. Then, the augmented objective function can be defined as

$$\bar{J}\left[\bar{\mathbf{d}}\left[\boldsymbol{\rho}\right],\boldsymbol{\rho}\right] = J\left[\bar{\mathbf{d}}\left[\boldsymbol{\rho}\right],\boldsymbol{\rho}\right] + \boldsymbol{\mu}^T\mathbf{R}^T\left(\mathbf{f} - \mathbf{q}\left[\bar{\mathbf{d}}\left[\boldsymbol{\rho}\right],\boldsymbol{\rho}\right]\right) + \sum_{j=1}^{m}\boldsymbol{\theta}_j^{\mathrm{T}}\left(\mathbf{f}_{\phi} - \mathbf{q}_{\phi}\left[\boldsymbol{\phi}_j\left[\boldsymbol{\rho}\right],\boldsymbol{\rho}\right]\right), \tag{34}$$

where m is the number of base vectors. Next, to improve readability, $\bar{\mathbf{d}}\left[\boldsymbol{\rho}\right]$ is compactly denoted by $\bar{\mathbf{d}}$ and $\boldsymbol{\phi}_j\left[\boldsymbol{\rho}\right]$ by $\boldsymbol{\phi}_j$.

Taking derivatives of Eq. (34) to design variables $\boldsymbol{\rho}$, we get

$$\begin{aligned}\frac{\mathrm{d}\bar{J}\left[\bar{\mathbf{d}},\boldsymbol{\rho}\right]}{\mathrm{d}\boldsymbol{\rho}} = {} & J_{,\bar{\mathbf{d}}}\left[\bar{\mathbf{d}},\boldsymbol{\rho}\right]\frac{\mathrm{d}\bar{\mathbf{d}}}{\mathrm{d}\boldsymbol{\rho}} + J_{,\boldsymbol{\rho}}\left[\bar{\mathbf{d}},\boldsymbol{\rho}\right] + \boldsymbol{\mu}^{\mathrm{T}}\frac{\mathrm{d}\mathbf{R}^{\mathrm{T}}}{\mathrm{d}\boldsymbol{\rho}}\left(\mathbf{f} - \mathbf{q}\left[\bar{\mathbf{d}},\boldsymbol{\rho}\right]\right) - \boldsymbol{\mu}^{\mathrm{T}}\mathbf{R}^{\mathrm{T}}\left(\mathbf{q}_{,\bar{\mathbf{d}}}\left[\bar{\mathbf{d}},\boldsymbol{\rho}\right]\frac{\mathrm{d}\bar{\mathbf{d}}}{\mathrm{d}\boldsymbol{\rho}} + \mathbf{q}_{,\boldsymbol{\rho}}\left[\bar{\mathbf{d}},\boldsymbol{\rho}\right]\right)\\ & - \sum_{j=1}^{m}\boldsymbol{\theta}_j^{\mathrm{T}}\left(\mathbf{q}_{\phi,\bar{\mathbf{d}}}\left[\boldsymbol{\phi}_j,\boldsymbol{\rho}\right]\frac{\mathrm{d}\boldsymbol{\phi}_j}{\mathrm{d}\boldsymbol{\rho}} + \mathbf{q}_{\phi,\boldsymbol{\rho}}\left[\boldsymbol{\phi}_j,\boldsymbol{\rho}\right]\right),\end{aligned} \tag{35}$$

where

$$\boldsymbol{\mu}^{\mathrm{T}}\frac{\mathrm{d}\mathbf{R}^{\mathrm{T}}}{\mathrm{d}\boldsymbol{\rho}} = \sum_{j=1}^{m}\mu_j\left(\frac{\mathrm{d}\boldsymbol{\phi}_j}{\mathrm{d}\boldsymbol{\rho}}\right)^{\mathrm{T}}. \tag{36}$$

and

$$\frac{\mathrm{d}\bar{\mathbf{d}}}{\mathrm{d}\boldsymbol{\rho}} = \frac{\mathrm{d}\mathbf{R}}{\mathrm{d}\boldsymbol{\rho}}\mathbf{y} + \mathbf{R}\frac{\mathrm{d}\mathbf{y}}{\mathrm{d}\boldsymbol{\rho}}, \tag{37}$$

$$\frac{\mathrm{d}\mathbf{R}}{\mathrm{d}\boldsymbol{\rho}}\mathbf{y} = \sum_{j=1}^{m}y_j\frac{\mathrm{d}\boldsymbol{\phi}_j}{\mathrm{d}\boldsymbol{\rho}}. \tag{38}$$

Then, the derivatives Eq. (35) can be expressed as

$$\begin{aligned}\frac{\mathrm{d}\bar{J}\left[\bar{\mathbf{d}},\boldsymbol{\rho}\right]}{\mathrm{d}\boldsymbol{\rho}} = {} & J_{,\boldsymbol{\rho}}\left[\bar{\mathbf{d}},\boldsymbol{\rho}\right] - \boldsymbol{\mu}^{\mathrm{T}}\mathbf{R}^{\mathrm{T}}\mathbf{q}_{,\boldsymbol{\rho}}\left[\bar{\mathbf{d}},\boldsymbol{\rho}\right] - \sum_{j=1}^{m}\boldsymbol{\theta}_j^{T}\mathbf{q}_{\phi,\boldsymbol{\rho}}\left[\boldsymbol{\phi}_j,\boldsymbol{\rho}\right]\\ & + \sum_{j=1}^{m}\left\{y_j\left(J_{,\bar{\mathbf{d}}}\left[\bar{\mathbf{d}},\boldsymbol{\rho}\right] - \boldsymbol{\mu}^{\mathrm{T}}\mathbf{R}^{\mathrm{T}}\mathbf{q}_{,\bar{\mathbf{d}}}\left[\bar{\mathbf{d}},\boldsymbol{\rho}\right]\right) + \mu_j\left(\mathbf{f} - \mathbf{q}\left[\bar{\mathbf{d}},\boldsymbol{\rho}\right]\right)^{\mathrm{T}} - \boldsymbol{\theta}_j^{\mathrm{T}}\mathbf{q}_{\phi,\bar{\mathbf{d}}}\left[\boldsymbol{\phi}_j,\boldsymbol{\rho}\right]\right\}\frac{\mathrm{d}\boldsymbol{\phi}_j}{\mathrm{d}\boldsymbol{\rho}}\\ & + \left(J_{,\bar{\mathbf{d}}}\left[\bar{\mathbf{d}},\boldsymbol{\rho}\right]\mathbf{R} - \boldsymbol{\mu}^{\mathrm{T}}\mathbf{R}^{\mathrm{T}}\mathbf{q}_{,\bar{\mathbf{d}}}\left[\bar{\mathbf{d}},\boldsymbol{\rho}\right]\mathbf{R}\right)\frac{\mathrm{d}\mathbf{y}}{\mathrm{d}\boldsymbol{\rho}}.\end{aligned} \tag{39}$$

The derivatives $\frac{\mathrm{d}\mathbf{y}}{\mathrm{d}\rho}$ are avoided if the adjoint variables $\boldsymbol{\mu}$ satisfy

$$\mathbf{R}^{\mathrm{T}}\mathbf{K}_{\mathrm{T}}\left[\bar{\mathbf{d}},\boldsymbol{\rho}\right]\mathbf{R}\boldsymbol{\mu} = \overline{\mathbf{K}}_{\mathrm{T}}\left[\bar{\mathbf{d}},\boldsymbol{\rho}\right]\boldsymbol{\mu} = \mathbf{R}^{\mathrm{T}}J_{,\bar{\mathbf{d}}}^{\mathrm{T}}\left[\bar{\mathbf{d}},\boldsymbol{\rho}\right]. \tag{40}$$

Here $\overline{\mathbf{K}}_{\mathrm{T}}\left[\bar{\mathbf{d}},\boldsymbol{\rho}\right]$ denotes the reduced tangent stiffness matrix. Since $\overline{\mathbf{K}}_{\mathrm{T}}\left[\bar{\mathbf{d}},\boldsymbol{\rho}\right]$ is only associated with a few reduced DoFs, the solution of Eq. (40) is conveniently obtained and will be evaluated in the final configuration. The tedious part is to eliminate the derivatives of the base vectors $\frac{\mathrm{d}\boldsymbol{\phi}_j}{\mathrm{d}\boldsymbol{\rho}}$. For this, the corresponding adjoint variables $\boldsymbol{\theta}_j$, for $j = 1, 2, \ldots, m$, have to satisfy

$$\mathbf{q}_{\phi,\bar{\mathbf{d}}}^{\mathrm{T}}\left[\boldsymbol{\phi}_j,\boldsymbol{\rho}\right]\boldsymbol{\theta}_j = \mathbf{K}_{\mathrm{T}}\left[\boldsymbol{\phi}_j,\boldsymbol{\rho}\right]\boldsymbol{\theta}_j = y_j\left(J_{,\bar{\mathbf{d}}}\left[\bar{\mathbf{d}},\boldsymbol{\rho}\right] - \boldsymbol{\mu}^{\mathrm{T}}\mathbf{R}^{\mathrm{T}}\mathbf{K}\left[\bar{\mathbf{d}},\boldsymbol{\rho}\right]\right)^{\mathrm{T}} + \mu_j\left(\mathbf{f} - \mathbf{q}\left[\bar{\mathbf{d}},\boldsymbol{\rho}\right]\right). \tag{41}$$

Note, the tangent stiffness matrix $\mathbf{K}_{\mathrm{T}}\left[\boldsymbol{\phi}_j,\rho\right]$ is related to FOMs. More specifically, it will be related to FOMs for previous designs and/or different load levels due to the proposed updating scheme. Hence, this adjoint formulation would call for availability of tangent stiffness matrices corresponding to other load levels and/or different designs.

Table 1
Definition of terms used in the numerical examples.

Name	Meaning
ONLY FOM	Exclusively FOM-based method
ROM*	ROMs without path derivatives and augmentation
$(\mathrm{ROM}^*)_\mathrm{f}$	The number of FOM-based correction updates in ROM* for each optimization step
$(\mathrm{ROM}^*)_\mathrm{r}$	The number of ROM-based updates in ROM* for each optimization step
ROM+A	ROMs with augmentation without path derivatives
$(\mathrm{ROM}+\mathrm{A})_\mathrm{f}$	The number of FOM-based correction updates in ROM+A for each optimization step
$(\mathrm{ROM}+\mathrm{A})_\mathrm{r}$	The number of ROM-based updates in ROM+A for each optimization step
ROM+A+P	ROMs with augmentation and path derivatives
$(\mathrm{ROM}+\mathrm{A}+\mathrm{P})_\mathrm{f}$	The number of FOM-based correction updates in ROM+A+P for each optimization step
$(\mathrm{ROM}+\mathrm{A}+\mathrm{P})_\mathrm{r}$	The number of ROM-based updates in ROM+A+P for each optimization step

Thus, it is not efficient to calculate these terms in the ROM-based sensitivities. Therefore, an approximated method is proposed, which ignores the derivatives of $\boldsymbol{\phi}_j$. This means that it is assumed that the dependency of $\boldsymbol{\phi}_j$ on $\boldsymbol{\rho}$ has a relative minor effect on the resulting sensitivities. Following this strategy, the approximated formulation is expressed as

$$\frac{\mathrm{d}J\left[\overline{\mathbf{d}},\boldsymbol{\rho}\right]}{\mathrm{d}\boldsymbol{\rho}} \approx -\boldsymbol{\mu}^{\mathrm{T}}\mathbf{R}^{\mathrm{T}}\mathbf{q}_{,\boldsymbol{\rho}}\left[\overline{\mathbf{d}},\boldsymbol{\rho}\right] + J_{,\boldsymbol{\rho}}\left[\overline{\mathbf{d}},\boldsymbol{\rho}\right]. \tag{42}$$

In Eq. (42), the adjoint variable $\boldsymbol{\mu}$ is computed using Eq. (40). This implies that we do not need previous tangent operators. Compared to CFSA, this strategy only needs a reduced-order linear analysis, which leads to computational efficiency.

6. Numerical examples

Several numerical examples involving shell elements and solid elements are studied in this section to evaluate the proposed ROM-based techniques. The shell elements applied in this paper are 6-node, 12-DOF triangle elements, which can describe finite rotations by a co-rotation formulation. More detail are provided in the work of Van Keulen and Booij [28]. The solid elements are standard 6-node, 12-DOF tetrahedral elements with one integration point.

In the numerical tests, the efficiency of ROMs is measured by counting the number of ROM-based Newton iterations (ROM-based updates) and FOM-based correction iterations (FOM-based correction updates) for each topology optimization step. These numbers are compared with the number of FOM-based Newton iterations (FOM-based updates) of an exclusively FOM-based strategy. To keep illustrations compact, several terms are defined in the Table 1.

6.1. Cylindrical shell

We embark on testing with a mildly nonlinear case to assess the effectiveness of the proposed ROMs. A cylindrical shell is shown in Fig. 3, where all details of the problem have been provided and the quantities involved have consistent dimensions. We consider four different strategies for topology optimization, including ROM+A+P, ROM+A, ROM*, and "ONLY FOM". A comparison of their efficiency is provided in Fig. 4. As observed in Fig. 4(a), "ONLY FOM" requires around 40 FOM-based updates every optimization step. Whereas, per optimization step, ROM* only requires 20 FOM-based updates and 60 ROM-based updates. Here, 60 ROM-based updates have negligible effect on efficiency since each ROM-based update only requires factorization of a small matrix in a 10×10 dimension. For further efficiency improvement, augmentation is included (See the result for ROM+A shown in Fig. 4(a)). Here, we can typically reduce the number of FOM-based updates to less than 20 per optimization step and logically, the number of ROM-based updates increases a bit to 60. Next, the impact of path derivatives is studied in Fig. 4(b). From the result, no obvious difference is obtained. It makes sense since path derivatives are mainly for inextensional bending structures, but this example is not the case.

Corresponding convergence curves of the four strategies are compared in Fig. 5. Evidently, all strategies underwent nearly the same optimization progress and converge to the same final result. This implies that the

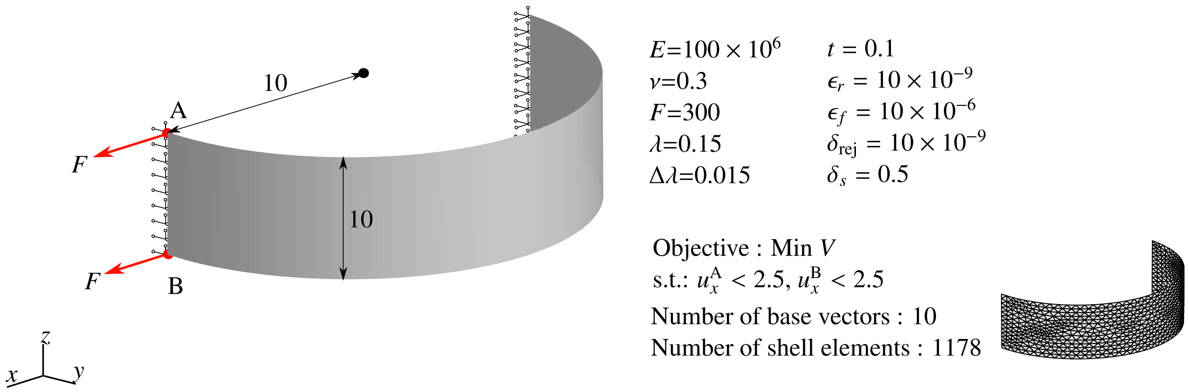

Fig. 3. Cylindrical shell. All quantities have consistent dimensions. Here, F denotes nodal forces applied at points A and B, t thickness, E Young's modulus, λ load factor, $\Delta\lambda$ increment of λ, ϵ_f the convergence tolerance for FOMs (See Eq. (15)), ϵ_r the convergence tolerance for ROMs (See Eq. (25)), δ_{rej} the rejection tolerance (See Section 4.3), δ_s the error tolerance for ROM-based results (See Section 4.1), V volume, u_x^{A} displacement of point A in x direction, and u_x^{B} displacement of point B in x direction.

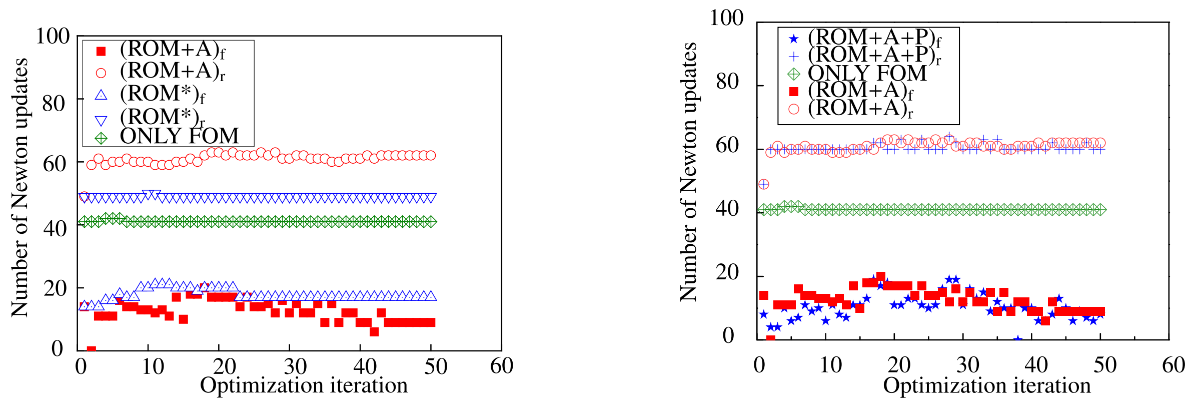

(a) Comparisionn between ROMs with and without augmentation

(b) Comparision between ROMs with and without path derivatives

Fig. 4. Efficiency test for the cylindrical model. The efficiency of ROMs is measured by counting the number of ROM-based updates and FOM-based correction updates for each topology optimization step. In the left picture, blue shapes denote ROMs without path derivatives and augmentation, where the up-pointing triangles are the number of ROM-based updates and the down-pointing triangles are corresponding FOM-based correction updates. The red shapes denote ROMs with augmentation without path derivatives, where the circles are ROM-based updates and the squares are FOM-based. In the right picture, the blue shapes represent ROMs with augmentation and path derivatives, where the starts are the number of ROM-based updates and the crosses are the corresponding FOM-based updates. The red shapes here are the same as the left picture. These numbers are compared with the number of FOM-based updates of exclusively FOM strategy, which are shown by the green points in both the left and right pictures. From the distribution of the points, we can see that ROMs with augmentation have better performance than ROMs with augmentation. The differences between ROMs with and without path derivatives are not distinct for this example. (For interpretation of the references to color in this figure legend, the reader is referred to the web version of this article.)

approximation we made in ROM-based sensitivity analysis, i.e. ARSA, has negligible impacts on the optimization progress and final result for this case. For details, we zoom in at an intermediate design of ROM+A+P, shown in Fig. 5, and look at its sensitivity of the constraint $u_x^{\text{A}} - 2.5 < 0$. The sensitivity value was obtained automatically by ARSA since the analysis ended with a ROM-based solution. As a comparison, we used FOMs to rerun the analysis for the same intermediate design and extracted CFSA values as shown in Fig. 5. According to the results, ARSA and CFSA provide a consistent sign but differing magnitudes. These differences did not obviously lead ROM-based optimization progress to a different way from the FOM-based one. It indicates that there are possibilities for optimization to ignore the errors existing in sensitivity values.

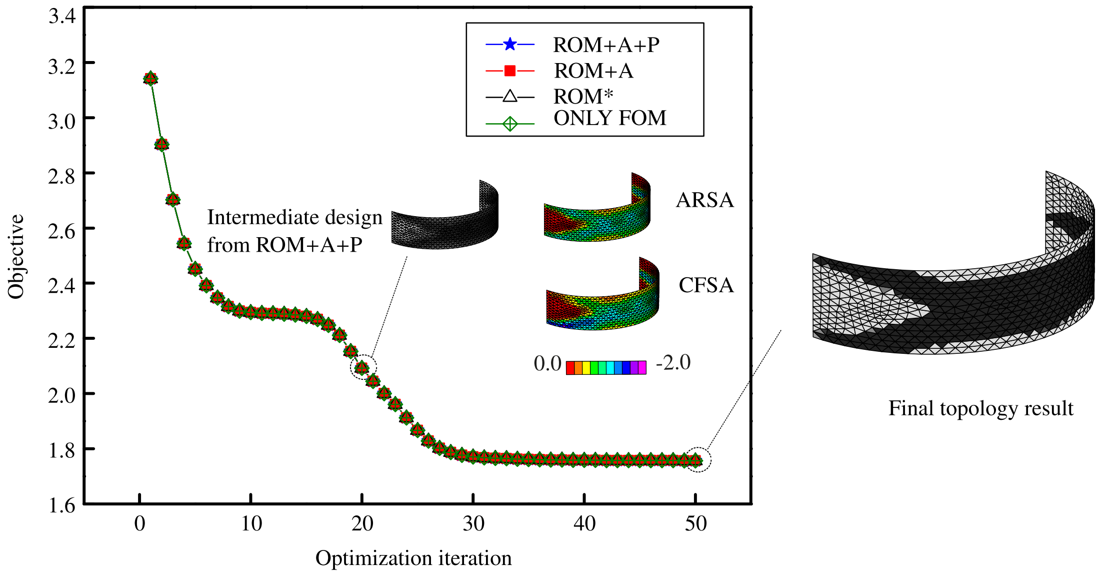

Fig. 5. Histories of objective values for the cylindrical model. For sensitivity evaluations, an intermediate design is selected from the optimization progress involving ROM+A+P method shown by the middle black–white figure. Focusing on this intermediate design, both ARSA and CFSA are used to calculate the sensitivity values of u_x^{A} with regard to all element pseudo densities. Different colors in ARSA and CFSA results represent sensitivity values. As observed, ARSA and CFSA provide consistent signs but differing magnitudes at some parts. These differences did not cause a big influence on the optimization progress and topology results. Both convergence and final design are similar. The final topology results for FOMs and ROMs are identically shown in the black–white figure on the right. (For interpretation of the references to color in this figure legend, the reader is referred to the web version of this article.)

6.2. Cantilever solid beam

A cantilever beam is depicted in Fig. 6. In this figure, all details of the problem have been provided and quantities involved have consistent dimensions. Given that the structure exhibits nearly inextensional bending behavior, it can highlight the importance of introducing path derivatives.

We consider four strategies including ROM*, ROM+A, ROM+A+P, and "ONLY FOM" for topology optimization. A comparison of their efficiency is shown in Fig. 7. First of all, we investigate the influences of augmentation; the results can be found in Fig. 7(a). As observed, the "ONLY FOM" method requires around 40 FOM-based updates, whereas ROM* only needs 10 FOM-based correction updates per optimization step. When augmentation is included, analyses are purely done by ROMs for 33 optimization steps and for the remaining 17 steps, no more than 10 correction updates are needed. Logically, decreasing the number of FOM-based correction updates results in a slight increase in ROM-based updates for ROM+A method. The increase hardly influences efficiency since in each ROM-based update, only a small matrix in a 10 × 10 dimension is factorized. After the introduction of path derivatives, as shown in Fig. 7(b), analyses are purely done by ROMs for 45 optimization steps and only 5 FOM-based correction updates are required in the remaining 5 optimization steps.

Corresponding convergence curves of the four strategies are compared in Fig. 8. In the figure, We zoom in at an intermediate design of ROM+A+P and look at its sensitivities for the constraint $-u_x^{\mathrm{A}} - 1.4 < 0$. Here the sensitivity was automatically obtained by ARSA since the analysis ended with a ROM-based solution. As a comparison, we then used FOMs to rerun the analysis for the same intermediate design and extracted CFSA values. According to the results, nearly identical SA values are obtained by ARSA and CFSA, and obviously lead to nearly the same optimization progress and topology result of the four strategies. The corresponding topology results can be found in Fig. 8.

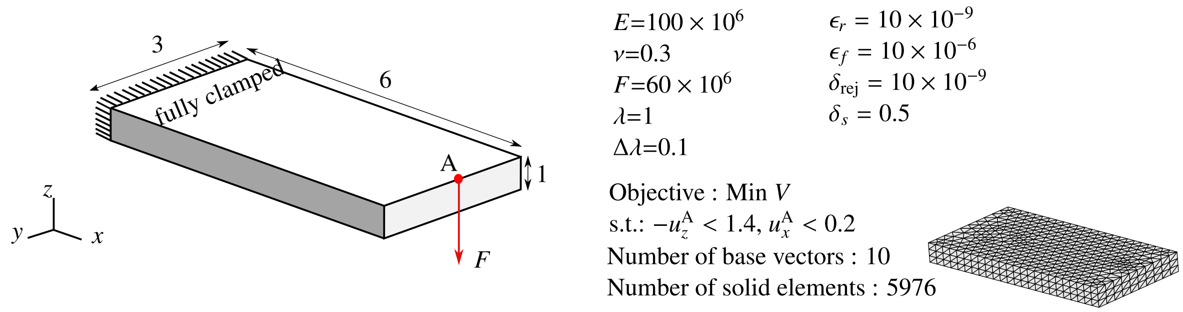

Fig. 6. Cantilever solid beam. All quantities have consistent dimensions. Here, F denotes a concentrate force applied to Point A, E Young's modulus, λ load factor, $\Delta\lambda$ load increment, ϵ_f the convergence tolerance for FOMs (See Eq. (15)), ϵ_r the convergence tolerance for ROMs (See Eq. (25)), δ_{rej} the rejection tolerance (See Section 4.3), δ_s the error tolerance for ROM-based results (See Section 4.1), V Volume, u_z^A displacement of Point A in z direction, and u_x^A displacement of Point A in x direction.

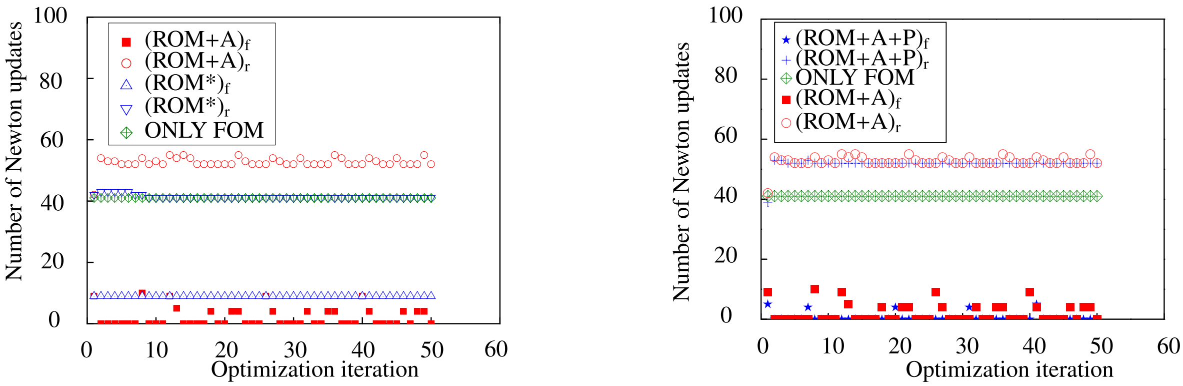

(a) Comparision between ROMs with and without augmentation

(b) Comparision between ROMs with and without path derivatives

Fig. 7. Efficiency test for the cantilever beam model. The efficiency of ROMs is measured by counting the number of ROM-based updates and FOM-based correction updates for each topology optimization step. In the left picture, blue shapes denote ROMs without path derivatives and augmentation, where the up-pointing triangles are the number of ROM-based updates and the down-pointing triangles are corresponding FOM-based correction updates. The red shapes denote ROMs with augmentation without path derivatives, where the circles are ROM-based updates and the squares are FOM-based. In the right picture, the blue shapes represent ROMs with augmentation and path derivatives, where the starts are the number of ROM-based updates and the crosses are the corresponding FOM-based updates. The red shapes here are the same as the left picture. These numbers are compared with the number of FOM-based updates of exclusively FOM strategy, which are shown by the green points in both the left and right pictures. From the comparison, ROM+A performs better than ROM*, and ROM+A+P further improves the efficiency compared to ROM+A. (For interpretation of the references to color in this figure legend, the reader is referred to the web version of this article.)

6.3. Thin plate model

A thin plate model is described in Fig. 9. In this figure, all details of the problem have been provided and quantities have consistent dimensions. In this example, we expect a very slender topology result where displacements can increase largely between two neighboring load steps. In this way, the advantage of augmentation technique can be clearly illustrated.

We use four strategies including ROM*, ROM+A, ROM+A+P, and "ONLY FOM" for topology optimization. The efficiency is compared in Fig. 10. First of all, we investigate the influences of augmentation and the results can be found in Fig. 10(a). As observed, the "ONLY FOM" method requires roughly 40 updates until the 20th optimization step. Thereafter, it increases to approximately 70 when the structure has become more slender. Similarly, after the 20th optimization step, ROM* intensively involves FOM-based correction updates. This inaccuracy is mainly due to large displacement changes between neighboring load steps. The situation can be improved by application of the augmentation technique. With augmentation from higher load levels of previous

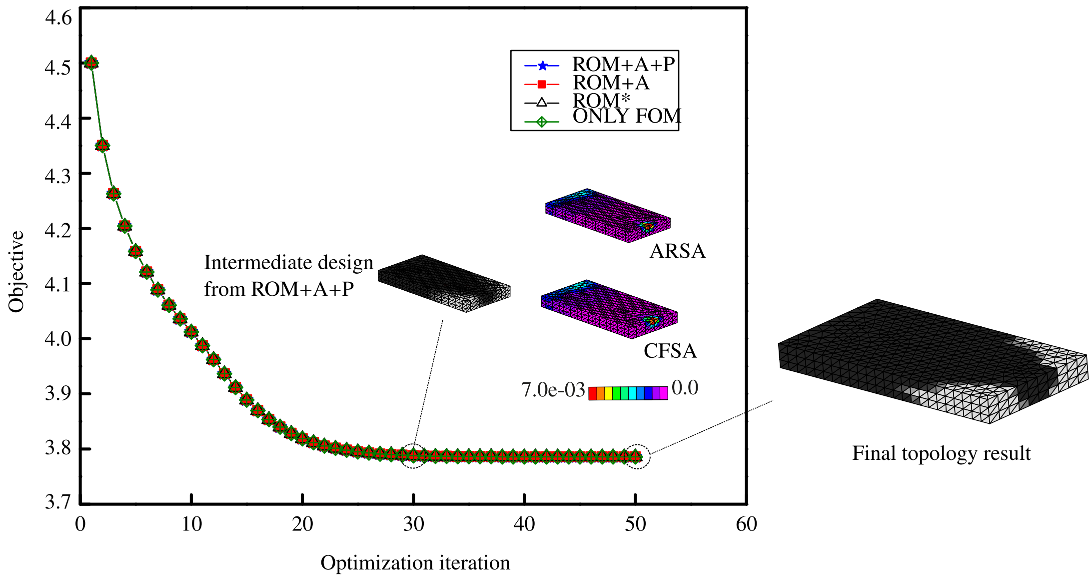

Fig. 8. Histories of objective values for the cantilever beam model. For sensitivity evaluations, an intermediate design is selected from the optimization progress involving ROM+A+P method shown by the middle black–white figure. Focusing on this intermediate design, both ARSA and CFSA are used to calculate the sensitivity values of $-u_z^A$ with regard to all element pseudo densities. Different colors in ARSA and CFSA results represent sensitivity values, where ARSA and CFSA provide nearly identical results and lead to the same result shown in the black–white figure on the right. (For interpretation of the references to color in this figure legend, the reader is referred to the web version of this article.)

designs, ROM+A needs fewer than 20 correction updates for the whole optimization progress. After involving path derivative, as shown in Fig. 10(b), although slightly, the efficiency can be further improved compared with ROM+A.

Corresponding convergence curves are compared in Fig. 11. In the figure, we zoom in at an intermediate design of ROM+A+P and look at its sensitivity of the constraint $u_z^A - 0.0015 < 0$. Here the sensitivity was automatically obtained by ARSA since the analysis ended with a ROM-based solution. As a comparison, we used FOMs to rerun the analysis for the same intermediate design and got CFSA values. According to the results, identical SA values are obtained by ARSA and CFSA, and obviously lead to the same optimization progress and topology result of the four strategies. The corresponding final topology is also shown in Fig. 11.

As is commonly understood, when a design exhibits mild nonlinearity, the differences between linear and nonlinear topologies may not be distinct. Thus, neglecting nonlinearity in the analysis may only lead to displacement errors but not an ineffective design. For relative high nonlinear cases, the differences between linear and nonlinear topologies could be obvious. For this thin plate case, we can observe a noticeable distinctions between the linear and nonlinear topologies shown in Fig. 12. In alignment with the nonlinear case, for the linear case, we minimize the volume while considering displacement constraints, but here the upper limit is established to be 100 times smaller than the nonlinear case. As illustrated in Fig. 12, the nonlinear case distributes the material uniformly along the symmetrical boundary, attempting to move away from the simply supported boundary to form a flexible strip, which can exhibit large deflections and rotations. For the linear case, the material is concentrated more towards the applied force, resulting in a design that is closely linked to the simply supported boundary. The results demonstrated that disregarding nonlinearity can result not only in displacement errors but also in a different design.

6.4. Spherical structure

A spherical structure is illustrated in Fig. 13. In this figure, all details of the problem have been provided and all quantities have consistent dimensions. The structure is separately discretized with shell elements and solid elements. We conducted topology optimization for both cases using the four strategies, and their efficiency and convergence results will be compared in the following subsections. Given that the structure exhibits nearly inextensional bending behavior, it can demonstrate the necessity of introducing path derivatives.

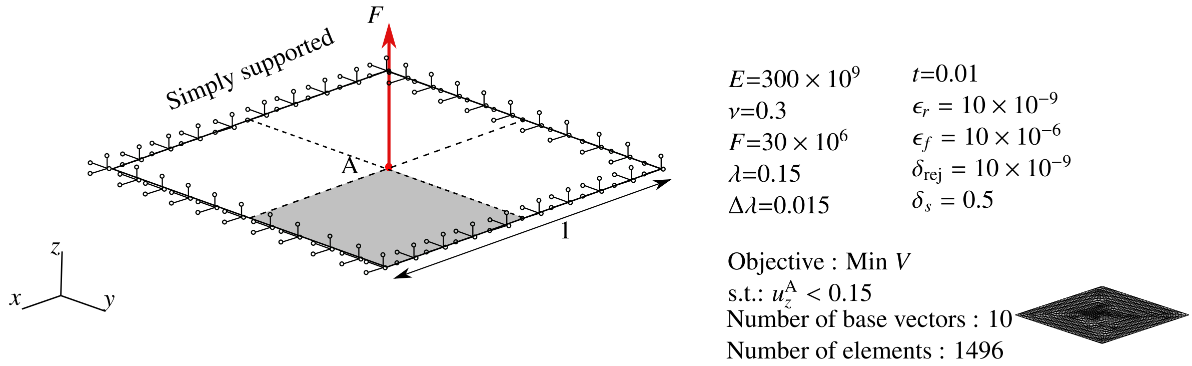

Fig. 9. Square thin plate. All quantities have consistent dimensions. Here, F denotes a concentrated force applied to Point A, t thickness, E Young's modulus, λ load factor, $\Delta\lambda$ increment of λ, ϵ_f the convergence tolerance for FOMs (See Eq. (15)), ϵ_r the convergence tolerance for ROMs (See Eq. (25)), δ_{rej} the rejection tolerance (See Section 4.3), δ_s the error tolerance for ROM-based results (See Section 4.1), V volume, and u_z^{A} displacement of Point A in z-direction. Due to symmetry, a quarter of the plate is selected for optimization.

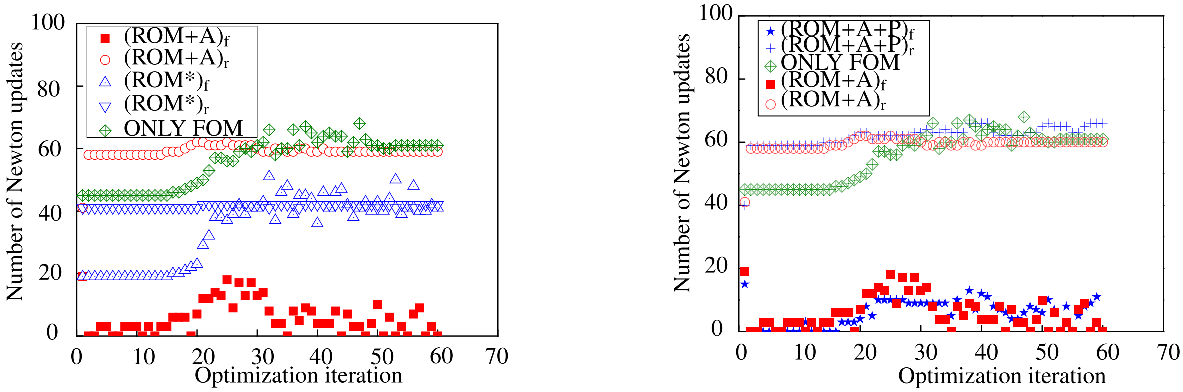

(a) comparision between ROMs with and without augmentation

(b) Comparison between ROMs with and without path derivatives

Fig. 10. Efficiency test for the thin plate. The efficiency of ROMs is measured by counting the number of ROM-based updates and FOM-based correction updates for each topology optimization step. In the left picture, blue shapes denote ROMs without path derivatives and augmentation, where the up-pointing triangles are the number of ROM-based updates and the down-pointing triangles are corresponding FOM-based correction updates. The red shapes denote ROMs with augmentation without path derivatives, where the circles are ROM-based updates and the squares are FOM-based. In the right picture, the blue shapes represent ROMs with augmentation and path derivatives, where the starts are the number of ROM-based updates and the crosses are the corresponding FOM-based updates. The red shapes here are the same as the left picture. These numbers are compared with the number of FOM-based updates of exclusively FOM strategy, which are shown by the green points in both the left and right pictures. From the comparison, ROM+A is obviously superior to ROM*. ROM+A+P performs slightly better than ROM+A. (For interpretation of the references to color in this figure legend, the reader is referred to the web version of this article.)

6.4.1. Spherical thin shell

For the structure meshed with shell elements shown in Fig. 13(b), we compare the efficiency of the four strategies in Fig. 14. First, we look into the effects of augmentation excluding path derivatives. The results can be found in Fig. 14(a). The "ONLY FOM" method performs stably, which requires roughly 70 updates per optimization step. For ROMs without augmentation, i.e. ROM*, it needs around 40 FOM-based and 80 ROM-based updates until the 20th optimization iteration. Thereafter, the number of both FOM-based and ROM-based updates becomes unstable. Especially, more than 80 FOM-based correction updates are required in the majority of optimization steps. After introducing the augmentation (See results of ROM+A), the number of ROM-based updates becomes much smaller compared to ROM*, but is still around and even exceeds 80. The efficiency can be improved further by introducing path derivatives. As shown in Fig. 14(b), ROMs with path derivatives and augmentation, i.e. ROM+A+P, can reduce the number of FOM-based correction updates to fewer than 40 for most optimization steps. However, the number

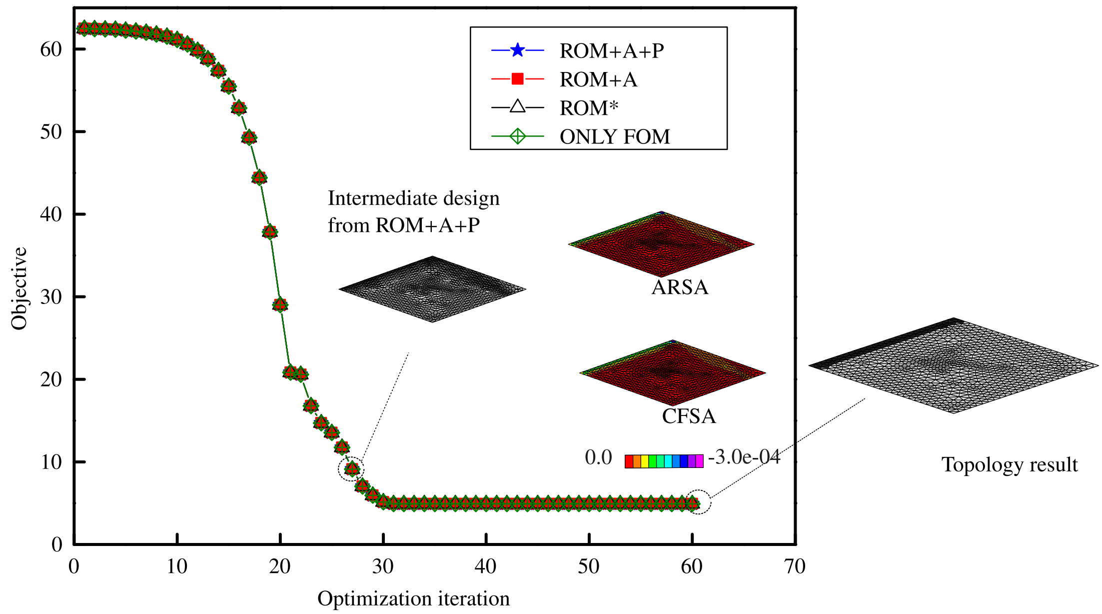

Fig. 11. Histories of objective values for the square thin plate model. For sensitivity evaluations, an intermediate design is selected from the optimization progress involving ROM+A+P method shown by the middle black–white figure. Focusing on this intermediate design, both ARSA and CFSA are used to calculate the sensitivity values of u_x^{A} with regard to all element pseudo densities. Different colors in ARSA and CFSA results represent sensitivity values, where ARSA and CFSA provide nearly identical results and lead to the same result shown in the black–white figure on the right. (For interpretation of the references to color in this figure legend, the reader is referred to the web version of this article.)

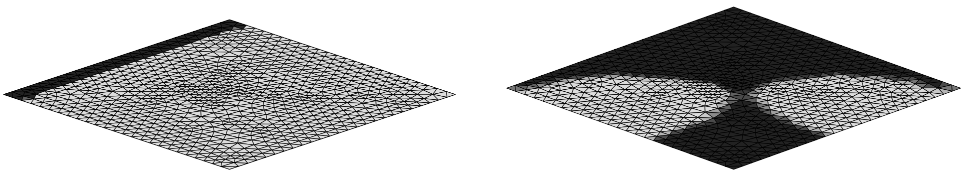

(a) Nonlinear result (b) Linear result

Fig. 12. Comparison between linear and nonlinear topology results for the thin plate model. For both cases, we minimize volume with displacement constraints. For the linear case, the upper limit of displacement constraint is 0.0015 but for the nonlinear case, it is 0.15. At the convergence, both displacement constraints are active.

of FOM-based corrections and ROM-based updates is still unstable. Particularly, at the 28th optimization step, we observe more than 100 FOM-based updates.

In order to understand the reasons behind the large number of FOM-based updates. We zoom in on the intermediate design at the 28th optimization step. Then, the ROM-based and the corrected FOM-based deformations at the last load incremental step are shown in Fig. 14(b). As observed, a local buckling mode is clearly visible in the middle low-density area of the ROM-based deformation figure. When looking at the corresponding FOM-based deformations, we observe a completely different local buckling mode. Given the differences, FOMs are intensively used to transfer the ROM-based one to the FOM-based one. To address this, in future work, techniques for refining ROMs need to be explored.

Corresponding convergence curves for the four strategies are shown in Fig. 15. As observed, ROM+A+P and ROM+A converge to the same objective value, which is slightly larger than the "ONLY FOM" result. The differences related to final topologies can be found in Fig. 15, which could result from the differences between ROM-based and FOM-based solutions, as well as the approximation introduced by the ROM-based sensitivity analysis method ARSA. The ARSA value of the constraint $-u_z^{\mathrm{A}} - 4 < 0$ for an intermediate design can be observed

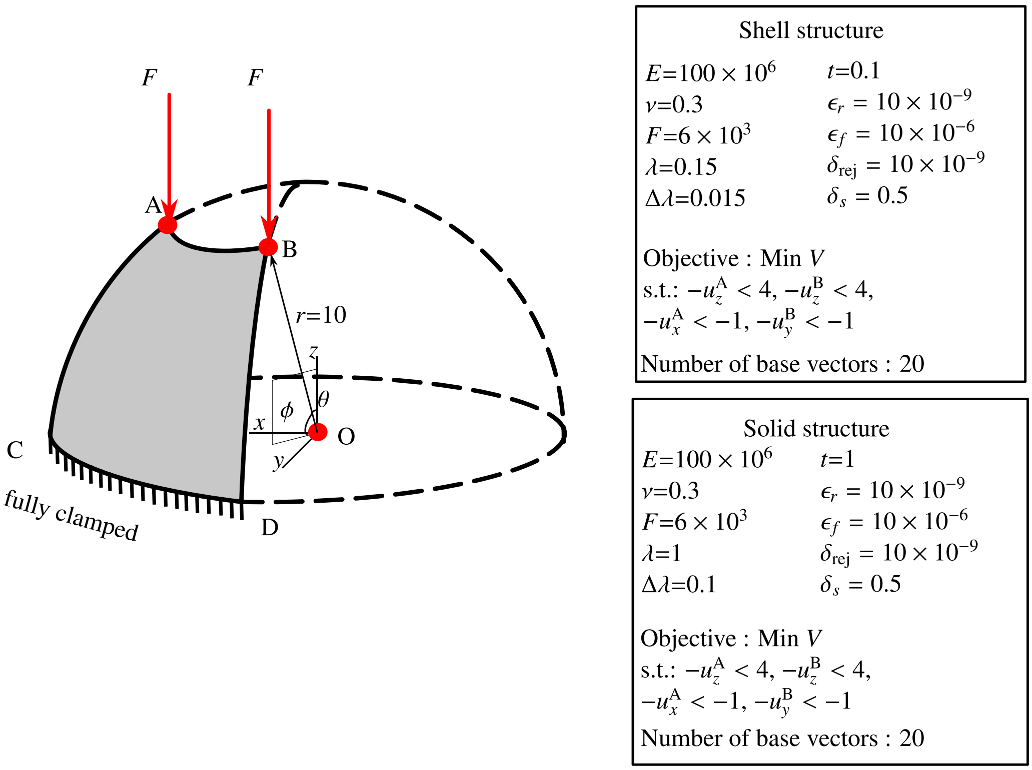

(a)

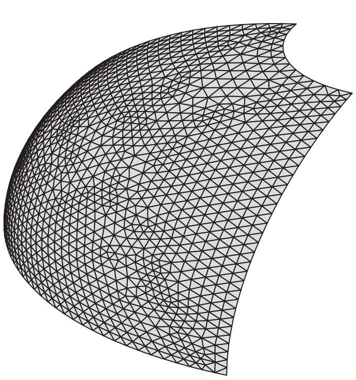

(b)

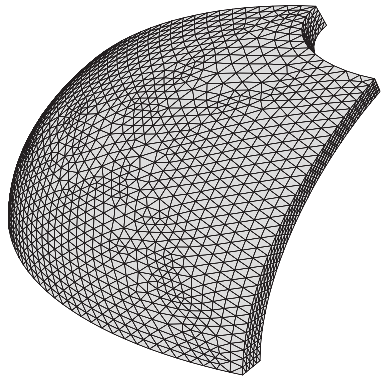

(c)

Fig. 13. Spherical structure and its meshes. (a) is the geometry. All quantities have consistent dimensions. Coordinates of Point A is $(r, \theta, \phi) = (10, \frac{2\pi}{5}, 0)$, Point B $(r, \theta, \phi) = (10, \frac{2\pi}{5}, \frac{\pi}{2})$, Point C $(r, \theta, \phi) = (10, \frac{\pi}{2}, 0)$, and Point D $(r, \theta, \phi) = (10, \frac{\pi}{2}, \frac{\pi}{2})$. Here, F denotes nodal forces applied to Point A and B, t thickness, E Young's modulus, λ load factor, $\Delta\lambda$ increment of λ, ϵ_f the convergence tolerance for FOMs (See Eq. (15)), ϵ_r the convergence tolerance for ROMs (See Eq. (25)), δ_{rej} the rejection tolerance (See Section 4.3), δ_s the error tolerance for ROM-based results (See Section 4.1), V Volume, u_z^A displacement of Point A in z direction, u_x^A displacement of Point A in x direction, u_z^B displacement of Point B in z direction, and u_x^B displacement of Point B in x direction. The model meshed with solid elements is shown in (b). The number of solid elements is 34 740. The model meshed with shell elements is shown in (c). The number of shell elements is 2316.

in Fig. 15. As a comparison, we reran the analysis using FOMs for the same intermediate design and got CFSA. Here CFSA and ARSA have the same sign but different magnitudes. These errors could lead to different results when structures become flexible. As for ROM*, it converges to nearly the same result as the "ONLY FOM" method. This would not be surprising after looking at the efficiency test (see Fig. 14(a)). Since the inaccuracy of ROM*,

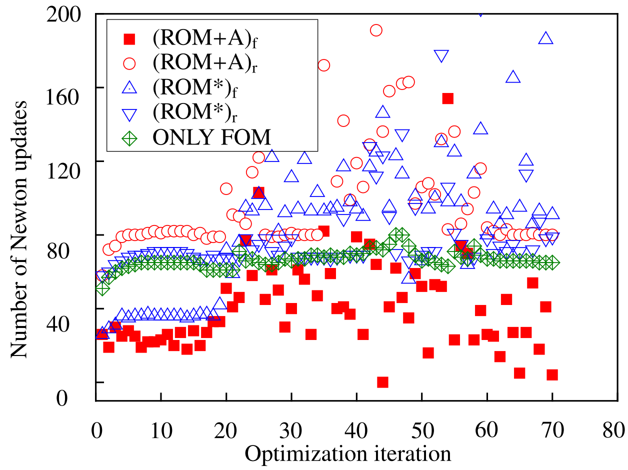

(a) Comparision between ROMs with and without augmentation

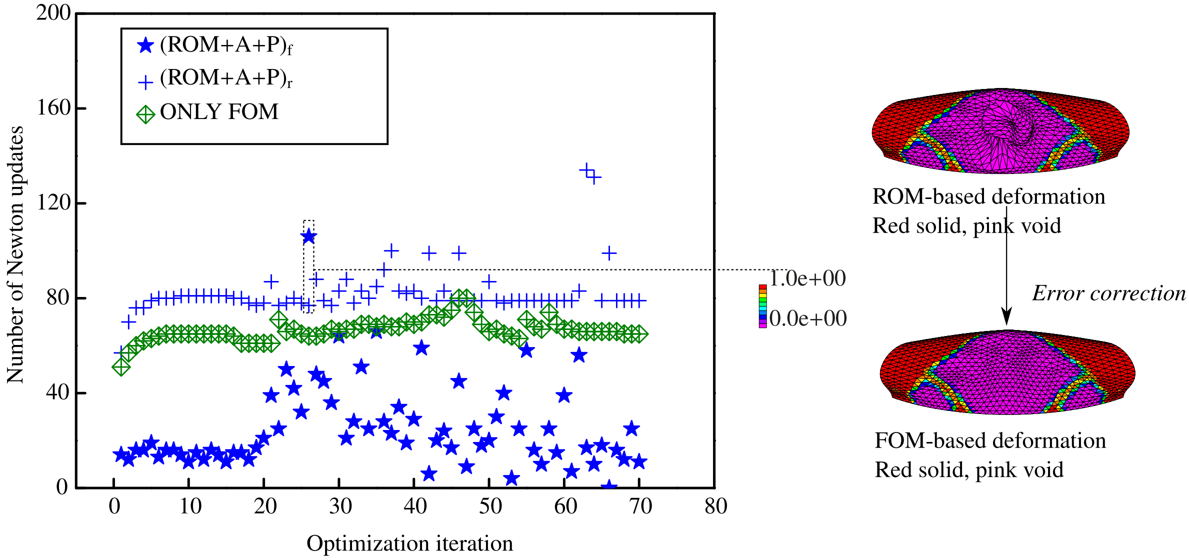

(b) Comparison between ROMs with and without path derivatives

Fig. 14. Efficiency test for the spherical thin shell. The efficiency of ROMs is measured by counting the number of ROM-based updates and FOM-based correction updates for each topology optimization step. In (a), blue shapes denote ROMs without path derivatives and augmentation, where the up-pointing triangles are the number of ROM-based updates and the down-pointing triangles are corresponding FOM-based correction updates. The red shapes denote ROMs with augmentation without path derivatives, where the circles are ROM-based updates and the squares are FOM-based. In (b), the blue shapes represent ROMs with augmentation and path derivatives, where the starts are the number of ROM-based updates and the crosses are the corresponding FOM-based updates. The red shapes here are the same as the left picture. These numbers are compared with the number of FOM-based updates of exclusively FOM strategy, which are shown by the green points in both (a) and (b). From the results, ROM+A performs better than ROM*, though both of them show extremely unstable update numbers. ROM+A+P has the best performance among the three ROM strategies. However, a large number of correction iterations are still observed. To understand this, an intermediate design is selected and ROM-based analysis is performed. Concerning the final load incremental step, corresponding ROM-based and the corrected FOM-based deformations are shown on the right. As observed, the ROM-based and FOM-based results show different local buckling modes. Thus, FOMs are intensively involved to transfer the ROM-based one to the FOM-based one.

nearly all of the load incremental steps ended with FOM-based solutions, and consequently, the optimization is led by CFSA instead of ARSA.

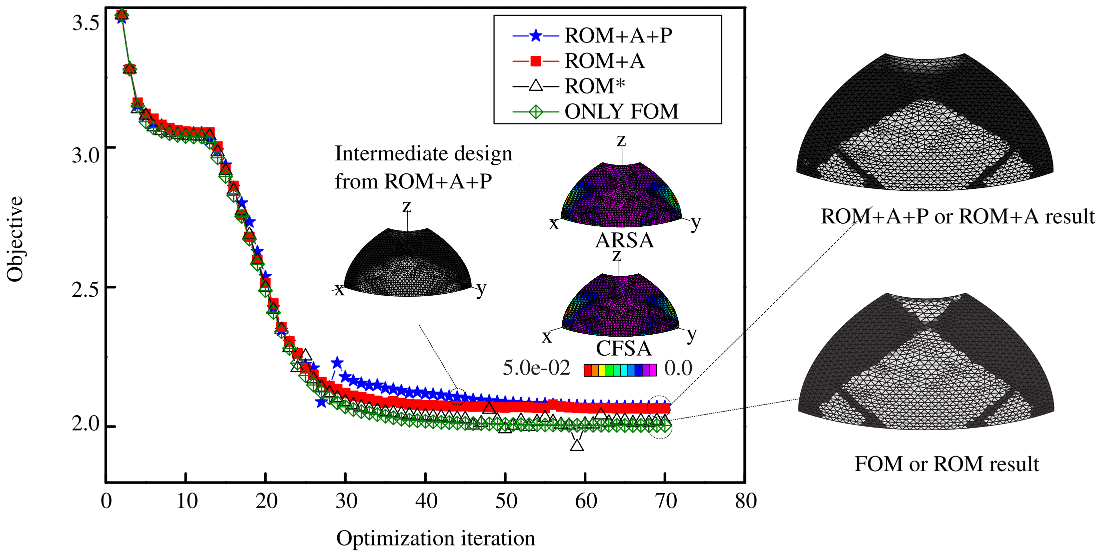

Fig. 15. Histories of objective values for the spherical thin shell model. An intermediate design is selected from the optimization progress involving ROM+A+P method shown by the middle black–white figure. Focusing on this intermediate design, both ARSA and CFSA are used to calculate the sensitivity values of $-u_z^{\mathrm{A}}$ with regard to all element pseudo densities. Different colors in ARSA and CFSA represent sensitivity values. Here ARSA and CFSA provide a consistent sign with differing magnitudes. These errors lead to slightly different results when the structure is flexible, which are illustrated by the black–white topology results shown on the right. Here, designs, at the 70th optimization steps, of ROM+A+P and ROM+A have a bit more material than the design of “ONLY FOM”. For ROM*, since its inaccuracy, nearly all of the load incremental steps ended with FOM-based solutions, and consequently, the optimization is led by CFSA instead of ARSA. Then, it converges to the same result as the “ONLY FOM” method.

6.4.2. Spherical solid shell

For the structure meshed with solid elements in Fig. 13(c), we compare the efficiency of the four strategies shown in Fig. 16. We start by examining the effects of augmentation and the results are shown in Fig. 16(a). Here, the “ONLY FOM” method requires roughly 50 updates for most optimization steps, however, increasing to more than 100 between the 20th and the 40th optimization step. We then zoom in on one of the intermediate designs and look at the deformation, see Fig. 16(a). As observed, the elements on the left bottom corner of the design are inside-out due to compression, which leads to convergence difficulties in the FOM-based analysis. The convergence difficulties in FOMs also have big influence on ROM*, since it intensively uses FOMs for both error correction and initialization at every optimization step. For ROM+A, the influence becomes less severe since the augmentation technique reduces the times of switching back to FOMs and avoids FOM-based initialization at every optimization step. Here only for three of the optimization steps, ROM+A requires more than 20 correction updates and the maximum number is about 40. If path derivatives are used (see Fig. 16(b)), a better result is obtained, though not distinctly. Here, the largest number of FOM-based correction updates is roughly 30.

The corresponding convergence curves are compared in Fig. 17. Although the four strategies went through different optimization progresses, they ultimately achieve similar objective values. ROM+A and ROM+A+P converge to nearly the same objective value, which is a bit larger than the one of “ONLY FOM”. The differences in topology can be seen on the right of Fig. 17, where more material appears in the middle of the ROM+A+P/ROM+A result. These variations could result from the differences between ROM-based and FOM-based solutions ($\delta_s = 0.5$), as well as the ARSA. The ARSA value of the constraint $-u_z^{\mathrm{A}} - 4 < 0$ for an intermediate design from ROM+A+P can be seen in Fig. 17. As a comparison, we then used FOMs to rerun the analysis for the same intermediate design and got CFSA values. According to the results, ARSA and CFSA provide a consistent sign but differing magnitudes. These errors could lead to differences in results when the structure is flexible. As for ROM*, since CFSA is frequently used due to its inaccurate ROM-based solutions, it converges to nearly the same result as the “ONLY FOM” method.

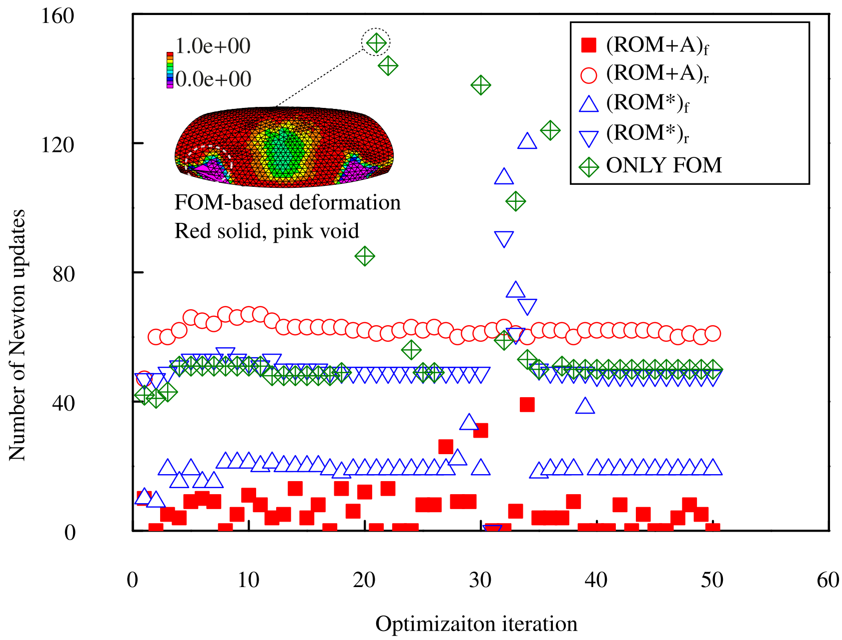

(a) Comparision between ROMs with and without augmentation

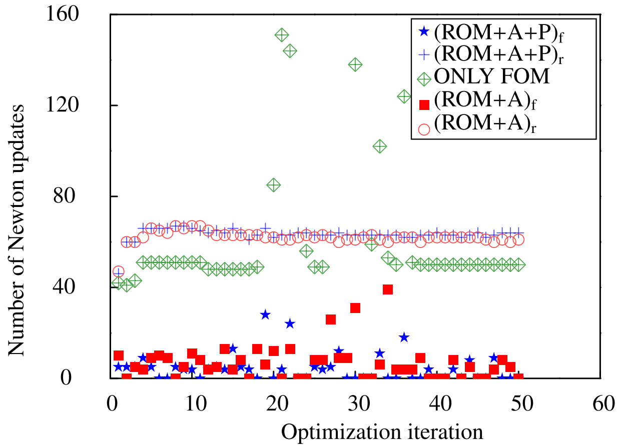

(b) ROMs with and without path derivatives

Fig. 16. Efficiency test for the spherical solid shell. The efficiency of ROMs is measured by counting the number of ROM-based updates and FOM-based correction updates for each topology optimization step. In (a), blue shapes denote ROMs without path derivatives and augmentation, where the up-pointing triangles are the number of ROM-based updates and the down-pointing triangles are corresponding FOM-based correction updates. The red shapes denote ROMs with augmentation without path derivatives, where the circles are ROM-based updates and the squares are FOM-based. In (b), the blue shapes represent ROMs with augmentation and path derivatives, where the starts are the number of ROM-based updates and the crosses are the corresponding FOM-based updates. The red shapes here are the same as the left picture. These numbers are compared with the number of FOM-based updates of exclusively FOM strategy, which are shown by the green points in both (a) and (b). From the results, the ONLY FOM method encounters divergence difficulties between the 20th and the 40th optimization steps. The reason is the instability of low-density elements as shown in the deformation figure. The convergence difficulties in FOMs have big influence on ROM* since it intensively uses FOMs for both error correction and initialization at every optimization step. For ROM+A, the influence becomes less severe since the augmentation technique improves accuracy and avoids FOM-based initialization at every optimization step. Then, if path derivatives are used, a better result than ROM+A is obtained, though the differences are not distinct.

7. Conclusions

This study introduces ROMs to improve the computing efficiency of incremental-iterative, geometrically nonlinear finite element simulations and the corresponding sensitivity analysis for topology optimization problems.

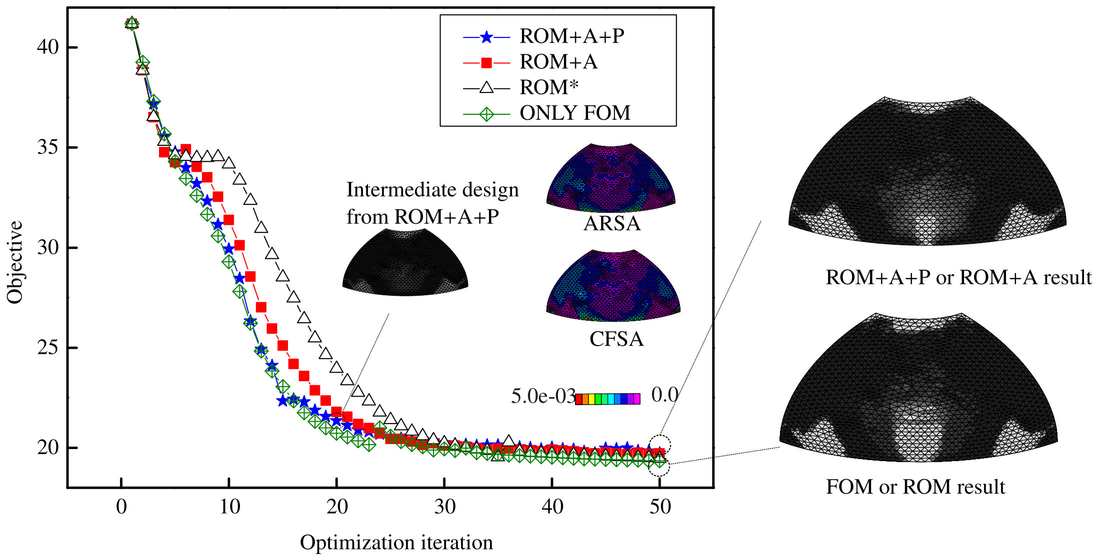

Fig. 17. Histories of objective values for the spherical solid shell. An intermediate design is selected from the optimization progress involving ROM+A+P method shown by the middle black–white figure. Focusing on this intermediate design, both ARSA and CFSA are used to calculate the sensitivity values of $-u_z^A$ with regard to all element pseudo densities. Different colors in ARSA and CFSA represent sensitivity values, where ARSA and CFSA provide a consistent sign with differing magnitudes. These errors lead to slightly different results when the structure is flexible, which are illustrated by the black–white topology results shown on the right. Here, designs, at the 50th optimization step, of ROM+A+P and ROM+A have a bit more material than the design of "ONLY FOM". As for ROM*, since CFSA is frequently used due to its inaccurate ROM-based solutions, it converges to nearly the same result as the "ONLY FOM" methods.

We have elaborately explained the initialization, update, error control, and augmentation techniques for the proposed ROMs. Besides, we have proposed approximated ROM-based sensitivity analysis strategies (ARSA) for practical and efficient use. Finally, the performance of the mentioned techniques has been examined by various geometrically nonlinear examples involving both solid as well as shell elements, and the results have been benchmarked against normal FOM-based ones.

Based on the findings, the proposed ROMs can effectively improve computing efficiency with a base vector number of no more than 20. Especially, with the augmentation from previous designs, the ROMs' efficiency can be greatly improved. Importantly, path derivatives are necessary for flexible structures; otherwise, ROM-based analysis lacks an effective description of flexible modes.

It is noticed that the ROM base also includes information from the void areas. As we use a Newton process, the displacements and rotations may be less accurate in void areas than in the solid domain. Given the fact that we need a basis which includes all nodal degrees of freedom, only selectively including nodal degrees of freedom is not an option. Moreover, it would increase complexity of the method significantly. Finally, the examples demonstrate that including all nodal degrees of freedom in the basis does not lead to complications. One issue caused by void areas could be spurious local buckling behavior shown in the spherical shell example. To address the issue, additional methodologies need to be employed, which is beyond the scope of the current paper.

With regard to sensitivities, we proposed an approximate ROM-based sensitivity analysis method (ARSA). Here, we ignore the gradients of base vectors from previous designs with regard to design variables and consequently, exclude previous tangent operators. In this way, we improve the efficiency of ROM-based sensitivity analysis. The suggested ARSA can successfully guide most cases to the same solution as obtained using a FOM-based formulation. However, for flexible structures, we observe slight differences between ROM-based and FOM-based topology results. The differences could result from the errors introduced by ROM-based solutions as well as the approximation brought in by ARSA.

Declaration of competing interest

The authors declare the following financial interests/personal relationships which may be considered as potential competing interests: Lidan Zhang reports financial support was provided by China Scholarship Council.

Data availability

Data will be made available on request.

Acknowledgments

The work is supported by China Scholarship Council.

Appendix A. Normalization

Gram–Schmidt orthogonalization is applied to obtain a well-conditioned ROM basis once a new base vector is introduced to the ROM basis. To illustrate the normalization progress, we start from an empty ROM basis $\mathbf{R} = []$. First, the bootstrapping process generates the FOM-based linear solution $\overline{\boldsymbol{\phi}}_{\mathbf{1}}$. Then we introduce it to $\mathbf{R}$. Since $\overline{\boldsymbol{\phi}}_{\mathbf{1}}$ is the only one in the basis, orthogonalization is not required. Then, $\boldsymbol{\phi}_{\mathbf{1}} = \overline{\boldsymbol{\phi}}_{\mathbf{1}}$ and $\mathbf{R} = [\boldsymbol{\phi}_{\mathbf{1}}]$. Here we use $\boldsymbol{\phi}$ to represent the base vector after orthogonalization.

Second, after the convergence of the FOM-based analysis, we introduce the FOM-based solution, i.e. $\overline{\boldsymbol{\phi}}_{\mathbf{2}}$, to the basis. Here we consider the ROMs without path derivatives for simple illustration. Now, the basis is not empty, we need to apply the orthogonalization. Since $\overline{\boldsymbol{\phi}}_{\mathbf{2}}$ is the latest vector, the corresponding deformation mode is closest to the current and the next load step. Given this, the vector is regarded as the start point of normalization, and the mode is completely maintained. Next, we remove $\overline{\boldsymbol{\phi}}_{\mathbf{2}}$ from $\overline{\boldsymbol{\phi}}_{\mathbf{1}}$, which means only the components orthogonal to $\overline{\boldsymbol{\phi}}_{\mathbf{1}}$ in $\overline{\boldsymbol{\phi}}_{\mathbf{2}}$ are attained. The orthogonalization can be explained by formulations

$$
\begin{aligned}
&\boldsymbol{\phi}_2 = \overline{\boldsymbol{\phi}}_2, \\
&\boldsymbol{\phi}_1 = \overline{\boldsymbol{\phi}}_1 - \frac{\langle \overline{\boldsymbol{\phi}}_1, \boldsymbol{\phi}_2 \rangle}{\langle \boldsymbol{\phi}_2, \boldsymbol{\phi}_2 \rangle} \boldsymbol{\phi}_2,
\end{aligned}
\tag{A.1}
$$

where $\langle \mathbf{a}, \mathbf{b} \rangle$ denotes the inner product of vectors $\mathbf{a}$ and $\mathbf{b}$. Then $\mathbf{R} = [\boldsymbol{\phi}_{\mathbf{1}}, \boldsymbol{\phi}_{\mathbf{2}}]$. Next, the $\mathbf{R}$ can be used for the ROM-based analysis. If FOM-based error correction is required, then we need to add a new FOM-based solution to the basis, i.e. base vector $\overline{\boldsymbol{\phi}}_3$. Following the same rules, we can get

$$
\begin{aligned}
&\boldsymbol{\phi}_3 = \overline{\boldsymbol{\phi}}_3, \\
&\boldsymbol{\phi}_2 = \overline{\boldsymbol{\phi}}_2 - \frac{\langle \overline{\boldsymbol{\phi}}_2, \boldsymbol{\phi}_3 \rangle}{\langle \boldsymbol{\phi}_3, \boldsymbol{\phi}_3 \rangle} \boldsymbol{\phi}_3, \\
&\boldsymbol{\phi}_1 = \overline{\boldsymbol{\phi}}_1 - \frac{\langle \overline{\boldsymbol{\phi}}_1, \boldsymbol{\phi}_2 \rangle}{\langle \boldsymbol{\phi}_2, \boldsymbol{\phi}_2 \rangle} \boldsymbol{\phi}_2 - \frac{\langle \overline{\boldsymbol{\phi}}_2, \boldsymbol{\phi}_3 \rangle}{\langle \boldsymbol{\phi}_3, \boldsymbol{\phi}_3 \rangle} \boldsymbol{\phi}_3,
\end{aligned}
\tag{A.2}
$$

Then $\mathbf{R} = [\boldsymbol{\phi}_{\mathbf{1}}, \boldsymbol{\phi}_{\mathbf{2}}, \boldsymbol{\phi}_{\mathbf{3}}]$. For each new base vector, we apply the same rule. Generally, if we assume at a specific load step, the corresponding ROM basis $\mathbf{R}$ before normalization with base vectors $[\overline{\boldsymbol{\phi}}_1 ... \overline{\boldsymbol{\phi}}_m]$, where $\overline{\boldsymbol{\phi}}_1$ is the first vector added to $\mathbf{R}$ and $\overline{\boldsymbol{\phi}}_m$ is the vector just added to $\mathbf{R}$. The Gram–Schmidt orthogonalization starts from $\overline{\boldsymbol{\phi}}_m$ and ends at $\overline{\boldsymbol{\phi}}_1$. The orthogonalized progress is shown by

$$
\begin{aligned}
&\boldsymbol{\phi}_m = \overline{\boldsymbol{\phi}}_m, \\
&\boldsymbol{\phi}_{m-1} = \overline{\boldsymbol{\phi}}_{m-1} - \frac{\langle \overline{\boldsymbol{\phi}}_{m-1}, \boldsymbol{\phi}_m \rangle}{\langle \boldsymbol{\phi}_m, \boldsymbol{\phi}_m \rangle} \boldsymbol{\phi}_m, \\
&\vdots \\
&\boldsymbol{\phi}_1 = \overline{\boldsymbol{\phi}}_1 - \frac{\langle \overline{\boldsymbol{\phi}}_1, \boldsymbol{\phi}_m \rangle}{\langle \boldsymbol{\phi}_m, \boldsymbol{\phi}_m \rangle} \boldsymbol{\phi}_m - \frac{\langle \overline{\boldsymbol{\phi}}_1, \boldsymbol{\phi}_{m-1} \rangle}{\langle \boldsymbol{\phi}_{m-1}, \boldsymbol{\phi}_{m-1} \rangle} \boldsymbol{\phi}_{m-1} - \cdots - \frac{\langle \overline{\boldsymbol{\phi}}_1, \boldsymbol{\phi}_2 \rangle}{\langle \boldsymbol{\phi}_2, \boldsymbol{\phi}_2 \rangle} \boldsymbol{\phi}_2,
\end{aligned}
\tag{A.3}
$$

In this way, a well-defined base vector is obtained and $\mathbf{R} = [\boldsymbol{\phi}_{\mathbf{1}}, \boldsymbol{\phi}_{\mathbf{2}}, \ldots, \boldsymbol{\phi}_{\mathbf{m}}]$.

Appendix B. ROMs for inextensional-bending structures

In order to accurately simulate structures subjected to nearly inextensional bending, path derivatives are taken into consideration for the ROM basis. In this section, the necessity of considering path derivatives for inextensional-bending structures is illustrated analytically. Next, the validity of path derivatives is highlighted by a numerical model.

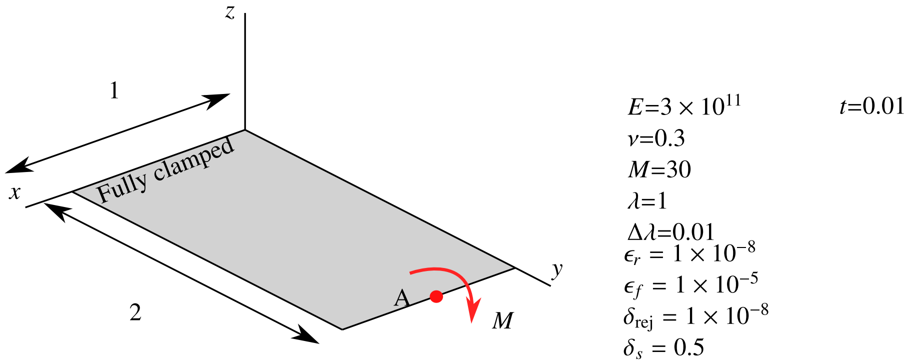

Fig. B.18. The pure-bending cantilever stripe. Here, E is Young's modulus, M a moment, t thickness, λ load factor, $\Delta\lambda$ increment of λ, ϵ_r the convergence tolerance of FOMs, ϵ_r the convergence tolerance of ROMs, δ_{rej} the rejection tolerance, and δ_s the error tolerance of ROM-based results.

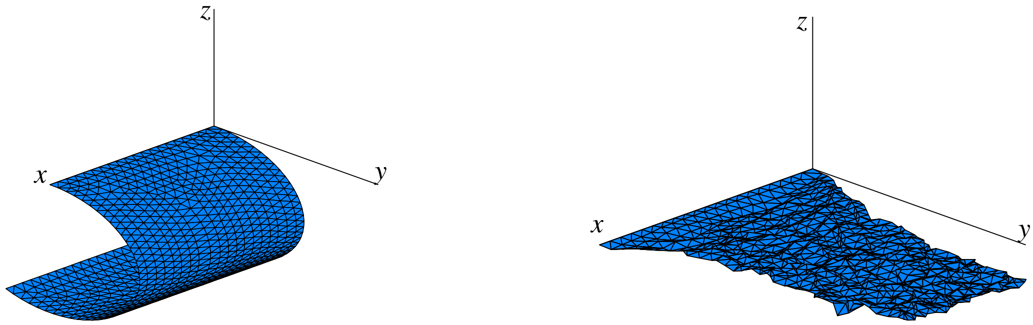

(a) FOM based result

(b) ROM-based result

Fig. B.19. Final FOM-based and ROM-based deformed configurations of the cantilever stripe.

B.1. A pure bending cantilever stripe model

In this section, we describe a cantilever plate, which is bent to a cylinder shell by the moment at the tip. The model is shown in Fig. B.18, where 100 load steps are involved in the analysis. At first, the normal FOM-based method is applied to the analysis and the deformed configuration at the last load step ($\lambda = 1$) is shown in Fig. B.19(a). The number of FOM iterations is 199. Then, ROMs without path derivatives are applied to the analysis. We observe that after the ROM-based analysis converges, FOM-based error correction is involved and convergence difficulties appear during progress. The reason for the latter is that the corresponding ROM-based result provides a bad start for FOM-based correction updates, and causes instabilities, shown in Fig. B.19(b), in the FOM-based correction progress. The bad start provided by ROMs is mainly because of artificial in-plane stiffness introduced by ROMs. In the next section, an analytical example is studied to better understand the problem.

B.2. Errors of ROMs in inextensional-bending structures

In order to understand artificial in-plane stiffness introduced by ROMs, a simple pure-bending problem for a cantilever beam is illustrated in Fig. B.20. For pure-bending condition, the curvature is a constant along the length:

$$\frac{1}{R} = \frac{M}{EI}, \tag{B.1}$$

where $\frac{1}{R}$ is curvature, M is the moment, and EI is the bending stiffness. Thus, the shape of the deformed configuration is a part of a circle with a radius of R. The displacement u along the x-axis and the displacement v

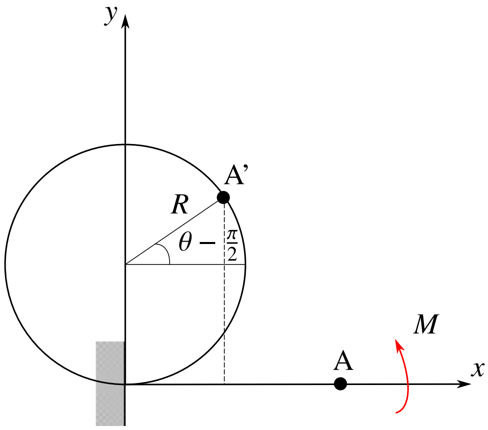

Fig. B.20. A pure-bending cantilever beam subjected to the moment M. The Point A moves to Point A' after bending. Here, R is the radius of curvature.

along the y-axis at arbitrary points of the beam can be defined by Eq. (B.2).

$$\begin{bmatrix} u \\ v \end{bmatrix} = \begin{bmatrix} R \cdot \sin\theta - x \\ R - R \cdot \cos\theta \end{bmatrix}, \tag{B.2}$$

with

$$\theta = \frac{x}{R}. \tag{B.3}$$

If we introduce non-dimension variables $\eta = \frac{x}{L}$ and $\alpha = \frac{L}{R}$, the Eq. (B.2) can be expressed by:

$$\begin{bmatrix} \frac{u}{L} \\ \frac{v}{L} \end{bmatrix} = \begin{bmatrix} -\eta(1 - \frac{\sin[\eta\alpha]}{\eta\alpha}) \\ \frac{1}{\alpha}(1 - \cos[\eta\alpha]) \end{bmatrix}. \tag{B.4}$$

Then, taking the solution Eq. (B.4) as the only base vector, we can construct a ROM basis $\mathbf{R} = \begin{bmatrix} \frac{u}{L} \\ \frac{v}{L} \end{bmatrix}$. Then a ROM-based solution based on the basis $\mathbf{R}$ can be described as

$$\begin{bmatrix} \frac{u}{L} \\ \frac{v}{L} \end{bmatrix}_{ROM} = C \begin{bmatrix} -\eta(1 - \frac{\sin[\eta\alpha]}{\eta\alpha}) \\ \frac{1}{\alpha}(1 - \cos[\eta\alpha]) \end{bmatrix}, \tag{B.5}$$

where C represents the generalized DOF. Next, we use the ratio between stretching energy and bending energy as the error measurement, since analytically, the stretching energy should be exactly zero for pure bending, and numerically, the stretching energy should be very small compared to the bending energy. If the ratio is relatively large, then errors should exist in our solutions. Thus, the error measurement can be defined by

$$\text{error} = \frac{W_{\text{stretching}}}{W_{\text{bending}}}. \tag{B.6}$$

Here, $W_{\text{stretching}}$ represents stretching energy and W_{bending} bending energy.

In the pure bending problem, W_{bending} can be obtained directly by

$$W_{\text{bending}} = \frac{1}{2}M\alpha = (\frac{1}{2})\frac{EI\alpha^2}{L}. \tag{B.7}$$

The stretching energy can be evaluated using the integration related to the bending stress σ_{11} and strain ϵ_{11}:

$$W_{\text{stretching}} = (\frac{1}{2})\int_V \sigma_{11}\epsilon_{11} dV = (\frac{1}{2})\int_{x=0}^{x=L} \sigma_{11}\epsilon_{11} A dx = (\frac{A}{2})\int_{\eta=0}^{\eta=1} \sigma_{11}\epsilon_{11} d\eta = (\frac{AE}{2})\int_{\eta=0}^{\eta=1} {\epsilon_{11}}^2 d\eta. \tag{B.8}$$

Thus, the error can be illustrated by

$$\text{error} = \frac{W_{\text{stretching}}}{W_{\text{bending}}} = (12\frac{L^2}{h^2})(\frac{1}{\alpha^2})\int_{\eta=0}^{\eta=1} {\epsilon_{11}}^2 d\eta. \tag{B.9}$$

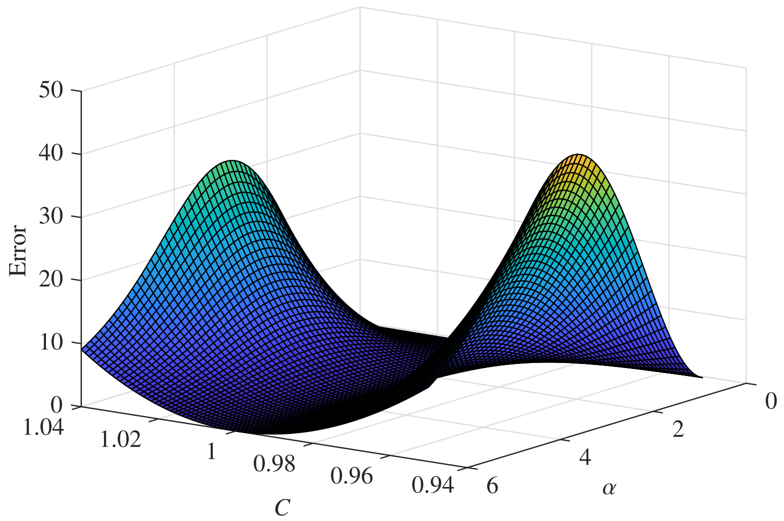

Fig. B.21. Strain energy error encountered by ROMs. C is generalized coordinates and α is curvature.

Since

$$\epsilon_{11} = \frac{\partial u}{\partial x} + \frac{1}{2}(\frac{\partial u}{\partial x})^2 + (\frac{\partial v}{\partial x})^2, \tag{B.10}$$

the integration in the Eq. (B.8) can be described by:

$$\int_{\eta=0}^{\eta=1} {\epsilon_{11}}^2 d\eta = \int_{\eta=0}^{\eta=1} (\cos(\alpha\eta) - 1)^2 (C - C^2)^2 d\eta = (\frac{1}{4\alpha}\sin(2\alpha) - \frac{2}{\alpha}\sin\alpha + \frac{3}{2})(C - C^2)^2. \tag{B.11}$$

Stretching energy should be zero for pure bending. However, according to Eq. (B.11), the stretching energy is a function of the generalized coordinate C when the ROM is applied. The relationship between C, α, and strain energy error is illustrated in Fig. B.21 where $L/h = 100$. Here, $C = 1$ means we use the base vector Eq. (B.4) to represent itself, and consequently, there are no errors. When $C \neq 1$, we intend to use the base vector Eq. (B.4) to represent nearby solutions, which is exactly the usual case in the ROM-based analysis. From the result, a subtle perturbation of C will substantially increase error, i.e. stretching energy. With a fixed $C \neq 1$, the error will reach the peak when the structure is bent to a half-circle, where α is between 3 and 4. The reason for the large stretching energy is that inextensional mode cannot be described by the base vector Eq. (B.4). The problem can be solved by introducing the 2nd order of path derivative in the ROM basis, which can give ROMs more information associated with the in-plane deformation.

B.3. FEA of the pure bending plate with path derivatives

The pure bending plate is tested again using ROMs with path derivatives. The maximum number of base vectors is 20. The analysis result is shown in Fig. B.22. The ROM-based analysis can converge with path derivatives, and the deformed configuration is the same as the FOM-based one. In the ROM-based method, the number of FOM solves is only 93, and the number of ROM solves is 299. Compared to the FOM-based method, where the number of FOM solves is 199, ROMs' efficiency is dramatically enhanced.

Concerning this model, we will discuss the feasibility of replacing the full Newton method with the modified Newton for path derivatives. At first, we analyze the plate model using ROMs involving the full Newton method. The corresponding number of ROM-based and FOM-based correction updates are illustrated in Table B.2. Here, we try different perturbation steps $\Delta\lambda^* = \Delta\lambda \times \epsilon$ by changing the perturbation parameter ϵ, where $\Delta\lambda$ is the load incremental step. We also consider different convergence tolerances ϵ_p in the perturbed displacement generation progress for path derivatives. The purpose is to define suitable ϵ and ϵ_p for the calculation. It can be seen in Table B.2, when $\epsilon = 1 \times 10^{-3}$ or 1×10^{-4}, we can obtain relative good results. Besides, similar to the finite

Table B.2
The number of Newton iterations involving ROMs, where path derivatives are calculated by full Newton method. In the table, ϵ is the perturbation, and ϵ_p is the convergence tolerance in the path-derivative calculation loop. The tolerance ϵ_f in the error correction loop is $1 * 10^{-5}$.

ϵ	ϵ_p	FOM	ROM
1e−3	1e−5	105	322
1e−3	1e−8	98	310
1e−4	1e−5	103	311
1e−4	1e−8	94	302
1e−6	1e−5	148	303
1e−6	1e−8	113	564

Table B.3
The number of Newton iterations involving ROMs, where path derivatives are calculated by modified Newton method. In the table, ϵ is the perturbation, and ϵ_p is the convergence tolerance in the path-derivative calculation loop. The tolerance ϵ_f in the error correction loop is $1 * 10^{-5}$.

ϵ	ϵ_p	FOM	ROM
1e−3	1e−5	136	253
1e−3	1e−8	97	268
1e−4	1e−5	131	262
1e−4	1e−8	93	299
1e−6	1e−5	157	396
1e−6	1e−8	106	565

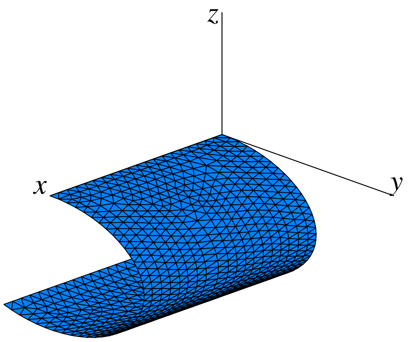

(a) FOM-based deformed configuration

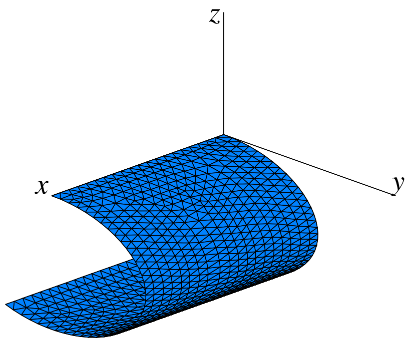

(b) ROM-based deformed configuration with path derivatives

Fig. B.22. Final FOM-based and ROM-based deformed configurations of the pure bending stripe.

difference method, too small a perturbation parameter ϵ cannot lead to better results. Moreover, we can see that a smaller ϵ_p can contribute to a better result.

Then, the same test is conducted with the modified Newton method and the results are shown in Table B.3. It can be seen that similar to full Newton, good results can be obtained by modified Newton when $\epsilon = 1 \times 10^{-3}$ or 1×10^{-4}. Considering the latter, when $\epsilon_p = 1 \times 10^{-8}$, the number of FOM-based correction updates involving the modified Newton is nearly the same as the full Newton. Thus, modified Newton is feasible to replace the full Newton method when a small tolerance ϵ_p is used for calculating perturbed displacements.

References

[1] M.P. Bendsøe, O. Sigmund, Material interpolation schemes in topology optimization, Arch. Appl. Mech. 69 (9–10) (1999) 635–654.
[2] N.P. van Dijk, K. Maute, M. Langelaar, F. Van Keulen, Level-set methods for structural topology optimization: a review, Struct. Multidiscip. Optim. 48 (3) (2013) 437–472.

[3] Y.M. Xie, G.P. Steven, A simple evolutionary procedure for structural optimization, Comput. Struct. 49 (5) (1993) 885–896.
[4] O. Querin, V. Young, G. Steven, Y. Xie, Computational efficiency and validation of bi-directional evolutionary structural optimisation, Comput. Methods Appl. Mech. Engrg. 189 (2000) 559–573.
[5] X. Guo, W. Zhang, W. Zhong, Doing topology optimization explicitly and geometrically—a new moving morphable components based framework, J. Appl. Mech. 81 (8) (2014) 081009.
[6] A. Polynkin, F. Van Keulen, V. Toropov, Optimization of geometrically nonlinear thin-walled structures using the multipoint approximation method, Struct. Optim. 9 (2) (1995) 105–116.
[7] H. Altenbach, O. Morachkovsky, K. Naumenko, A. Sychov, Geometrically nonlinear bending of thin-walled shells and plates under creep-damage conditions, Arch. Appl. Mech. 67 (5) (1997) 339–352.
[8] Z. Luo, L. Tong, A level set method for shape and topology optimization of large-displacement compliant mechanisms, Internat. J. Numer. Methods Engrg. 76 (6) (2008) 862–892.
[9] B.S. Lazarov, M. Schevenels, O. Sigmund, Robust design of large-displacement compliant mechanisms, Mech. Sci. 2 (2) (2011) 175–182.
[10] T. Bruns, O. Sigmund, D.A. Tortorelli, Numerical methods for the topology optimization of structures that exhibit snap-through, Internat. J. Numer. Methods Engrg. 55 (10) (2002) 1215–1237.
[11] K.-J. Bathe, Finite element method, in: Wiley Encyclopedia of Computer Science and Engineering, American Cancer Society, ISBN: 9780470050118, 2008, pp. 1–12, http://dx.doi.org/10.1002/9780470050118.ecse159, arXiv:https://onlinelibrary.wiley.com/doi/pdf/10.1002/9780470050118.ecse159, URL https://onlinelibrary.wiley.com/doi/abs/10.1002/9780470050118.ecse159.
[12] N.P. van Dijk, M. Langelaar, F. van Keulen, Element deformation scaling for robust geometrically nonlinear analyses in topology optimization, Struct. Multidiscip. Optim. 50 (4) (2014) 537–560.
[13] R.D. Lahuerta, E.T. Simões, E.M. Campello, P.M. Pimenta, E.C. Silva, Towards the stabilization of the low density elements in topology optimization with large deformation, Comput. Mech. 52 (4) (2013) 779–797.
[14] T.E. Bruns, D.A. Tortorelli, An element removal and reintroduction strategy for the topology optimization of structures and compliant mechanisms, Internat. J. Numer. Methods Engrg. 57 (10) (2003) 1413–1430.
[15] G. Xingjun, M. Haitao, Topology optimization of continuum structures under buckling constraints, Comput. Struct. 157 (2015) 142–152.
[16] N. Pedersen, Maximization of eigenvalues using topology optimization, Struct. Multidiscip. Optim. 20 (2000) 2–11.
[17] J. Zhao, W. Chunjie, Geometrically nonlinear finite element behaviour using buckling mode superposition, Comput. Methods Appl. Mech. Engrg. 53 (2016) 101–114.
[18] D. Nagy, M. König, Geometrically nonlinear finite element behaviour using buckling mode superposition, Comput. Methods Appl. Mech. Engrg. 19 (1979) 447–484.
[19] A.S.L. Chan, K.M. Hsiao, Nonlinear analysis using a reduced number of variables, Comput. Methods Appl. Mech. Engrg. 52 (1) (1985) 899–913.
[20] A. Safjan, Nonlinear structural analysis via reduced basis technique, Comput. Struct. 29 (6) (1988) 1055–1061.
[21] K. Kim, A.G. Radu, X.Q. Wang, M.P. Mignolet, Nonlinear reduced order modeling of isotropic and functionally graded plates, Int. J. Non-Linear Mech. 49 (2013) 100–110.
[22] O. Amir, M.P. Bendsøe, O. Sigmund, Approximate reanalysis in topology optimization, Internat. J. Numer. Methods Engrg. 78 (12) (2009) 1474–1491.
[23] C. Gogu, Improving the efficiency of large scale topology optimization through on-the-fly reduced order model construction, Internat. J. Numer. Methods Engrg. 101 (4) (2015) 281–304.
[24] E. Hooijkamp, F.v. Keulen, Topology optimization for linear thermo-mechanical transient problems: Modal reduction and adjoint sensitivities, Internat. J. Numer. Methods Engrg. 113 (8) (2018) 1230–1257.
[25] S. Wang, E. de Sturler, G. Paulino, Large-scale topology optimization using preconditioned krylov subspace methods with recycling, Internat. J. Numer. Methods Engrg. 69 (12) (2007) 2441–2468.
[26] L. Xia, P. Breitkopf, A reduced multiscale model for nonlinear structural topology optimization, Comput. Methods Appl. Mech. Engrg. 280 (2014) 117–134.
[27] C.E. Orozco, O.N. Ghattas, A reduced SAND method for optimal design of non-linear structures, Internat. J. Numer. Methods Engrg. 40 (15) (1997) 2759–2774.
[28] F. Van Keulen, J. Booij, Refined consistent formulation of a curved triangular finite rotation shell element, Internat. J. Numer. Methods Engrg. 39 (16) (1996) 2803–2820.